

# The VMC Survey - XXXII. Pre-main-sequence populations in the Large Magellanic Cloud

Viktor Zivkov<sup>1,2</sup>, Joana M. Oliveira<sup>1</sup>, Monika G. Petr-Gotzens<sup>2</sup>, Maria-Rosa L. Cioni<sup>3</sup>, Stefano Rubele<sup>4,5</sup>, Jacco Th. van Loon<sup>1</sup>, Kenji Bekki<sup>6</sup>, Felice Cusano<sup>7</sup>, Richard de Grijs<sup>8,9,10</sup>, Valentin D. Ivanov<sup>2</sup>, Marcella Marconi<sup>11</sup>, Florian Niederhofer<sup>3</sup>, Vincenzo Ripepi<sup>11</sup>, Ning-Chen Sun<sup>12</sup>

<sup>1</sup> Lennard-Jones Laboratories, School of Chemical and Physical Sciences, Keele University, ST5 5BG, UK

<sup>2</sup> European Southern Observatory, Karl-Schwarzschild-Str. 2, 85748 Garching bei München, Germany

<sup>3</sup> Leibniz-Institut für Astrophysik Potsdam, An der Sternwarte 16, D-14482 Potsdam, Germany

<sup>4</sup> Dipartimento di Fisica e Astronomia, Università di Padova, Vicolo dell'Osservatorio 2, I-35122 Padova, Italy

<sup>5</sup> Osservatorio Astronomico di Padova – INAF, Vicolo dell'Osservatorio 5, I-35122 Padova, Italy

<sup>6</sup> ICRAR, M468, University of Western Australia, 35 Stirling Hwy, 6009 Crawley, Western Australia, Australia

<sup>7</sup> INAF-Osservatorio di Astrofisica e Scienza dello Spazio di Bologna, Via P. Gobetti 93/3, I-40129 Bologna, Italy

<sup>8</sup> Department of Physics and Astronomy, Macquarie University, Balaclava Road, Sydney, NSW 2109, Australia

<sup>9</sup> Research Centre for Astronomy, Astrophysics and Astrophotonics, Macquarie University, Balaclava Road, Sydney, NSW 2109, Australia

<sup>10</sup> International Space Science Institute–Beijing, 1 Nanertiao, Zhongguancun, Hai Dian District, Beijing 100190, China

<sup>11</sup> INAF-Osservatorio Astronomico di Capodimonte, via Moiariello 16, 80131, Naples, Italy

<sup>12</sup> Kavli Institute for Astronomy & Astrophysics and Department of Astronomy, Peking University, Yi He Yuan Lu 5, Hai Dian District, Beijing 100871, China

## ABSTRACT

**Context.** Detailed studies of intermediate- and low-mass pre-main-sequence (PMS) stars outside the Galaxy have so far been conducted only for small targeted regions harbouring known star formation complexes. The VISTA Survey of the Magellanic Clouds (VMC) provides an opportunity to study PMS populations down to solar masses on a galaxy-wide scale.

**Aims.** Our goal is to use near-infrared data from the VMC survey to identify and characterise PMS populations down to  $\sim 1 M_{\odot}$  across the Magellanic Clouds. We present our colour–magnitude diagram method, and apply it to a  $\sim 1.5 \text{ deg}^2$  pilot field located in the Large Magellanic Cloud.

**Methods.** The pilot field is divided into equal-size grid elements. We compare the stellar population in every element with the population in nearby control fields by creating  $K_s/(Y-K_s)$  Hess diagrams; the observed density excesses over the local field population are used to classify the stellar populations.

**Results.** Our analysis recovers all known star formation complexes in this pilot field (N 44, N 51, N 148, and N 138) and for the first time reveals their true spatial extent. In total, around 2260 PMS candidates with ages  $\leq 10 \text{ Myr}$  are found in the pilot field. PMS structures, identified as areas with a significant density excess of PMS candidates, display a power-law distribution of the number of members with a slope of  $-0.86 \pm 0.12$ . We find a clustering of the young stellar populations along ridges and filaments where dust emission in the far-infrared (FIR) ( $70 \mu\text{m} - 500 \mu\text{m}$ ) is bright. Regions with young populations lacking massive stars show a lower degree of clustering and are usually located in the outskirts of the star formation complexes. At short FIR wavelengths ( $70 \mu\text{m}, 100 \mu\text{m}$ ) we report a strong dust emission increase in regions hosting young massive stars, which is less pronounced in regions populated only by less massive ( $\leq 4 M_{\odot}$ ) PMS stars.

**Key words.** techniques: photometric – galaxies: individual: LMC – galaxies: star formation – stars: statistics – stars: pre-main sequence

## 1. Introduction

The Magellanic Clouds (MCs) are nearby, interacting, gas-rich galaxies with metallicities lower than typically encountered in the Milky Way (Stanimirović et al. 2004; Besla et al. 2012). With moderate distances of  $50 \pm 2 \text{ kpc}$  for the Large Magellanic Cloud (LMC; de Grijs et al. 2014) and  $61.9 \pm 0.6 \text{ kpc}$  for the Small Magellanic Cloud (SMC; de Grijs & Bono 2015), they provide a great opportunity to study resolved star formation down to the scales of individual young stellar objects under different environmental conditions than those found in the Galaxy. The LMC has an apparent size on the sky of approximately  $5.4^{\circ} \times 4.6^{\circ}$  (Cook et al. 2014) and is seen almost face-on (van der Marel & Cioni

2001). Its depth is  $4.0 \pm 1.4 \text{ kpc}$  and  $3.44 \pm 1.16 \text{ kpc}$  in the bar region and the disc, respectively (Subramanian & Subramanian 2009), leading to relatively small distance modulus variations among its stellar members. The mean metallicity of the LMC is approximately half of the solar metallicity (Russell & Dopita 1992), which places it close to the mean metallicity of the interstellar medium during the time of peak star formation in the Universe (Pei et al. 1999).

The first studies of young stellar populations within the MCs were published over half a century ago (Westerlund 1961; Bok 1964). Lucke & Hodge (1970) created a catalogue of 122 OB associations in the LMC, based on observations at optical wavelengths down to  $m_V \approx 16 \text{ mag}$ , which corresponds at the LMC

distance to an  $\sim 11 M_{\odot}$  main-sequence star of age 10 Myr (Bresnan et al. 2012). The advent of sensitive CCD detector arrays improved the detection limit so that more detailed studies of the stellar content of associations became possible (e.g. Massey et al. 1989a,b). A huge leap in sensitivity and resolution was provided by the *Hubble Space Telescope* (HST). Optical imaging studies of young clusters and OB associations in both galaxies have found evidence of extensive pre-main-sequence (PMS) populations well below the solar mass regime (e.g. Gilmozzi et al. 1994; Panagia et al. 2000; Gouliermis et al. 2006a,b, 2007, 2011). Analysis of the PMS populations in the 30 Doradus region, revealed by the Hubble Tarantula Treasury Project (HTTP; Sabbi et al. 2013), allowed Cignoni et al. (2015) to reconstruct the star formation history of the complex. They also reported that low-mass stars can form in starburst regions as well as in low-density environments. Overall, the observed initial mass function (IMF) in the LMC is consistent with that of the Galaxy (e.g. Da Rio et al. 2009; Liu et al. 2009a,b). Spezzi et al. (2012) and De Marchi et al. (2013) used narrow-band photometry with an  $H\alpha$ -filter to identify PMS objects actively undergoing mass accretion. Both studies found that PMS stars in the MCs have higher mass accretion rates than stars of similar mass in the Galaxy, which might be an effect of metallicity. All these HST-studies targeted individual associations and/or star-forming complexes, uncovering the young stellar populations down to masses as low as  $\sim 0.3 M_{\odot}$ .

In contrast, large-scale photometric surveys of the LMC and/or SMC give a galaxy-wide overview of the stellar populations. They allow investigating the large-scale distribution of star-forming complexes and their relationship with the underlying gas and dust distribution. Optical imaging was performed by the Magellanic Cloud Photometric Survey (MCPS; Zaritsky et al. 2002, 2004), and near-infrared (NIR) images were provided by the 2 Micron All Sky Survey (2MASS; Skrutskie et al. 2006). Mid- and far-infrared (MIR, FIR) imaging was performed by the Spitzer Space Telescope (*Spitzer*; Werner et al. 2004) and the Herschel Space Observatory (*Herschel*; Pilbratt et al. 2010) as part of two legacy surveys (SAGE and SAGE-SMC; Meixner et al. 2006; Gordon et al. 2011; HERITAGE; Meixner et al. 2013). These surveys provided a comprehensive overview of the high-mass young stellar content and their spatial distribution, but they lack the depth and resolution for studying the intermediate- and low-mass young stellar population.

The VISTA Survey of the Magellanic Clouds (VMC; Cioni et al. 2011) provides a significant improvement in depth and resolution. Its data are being used, amongst other works, to characterise the stellar content of the MCs. Piatti et al. (2014) analysed the colour–magnitude diagrams (CMDs) of known clusters in the LMC, while Piatti et al. (2016) used stellar overdensities to detect new stellar clusters in the SMC with ages between  $\log(t/\text{yr}) \sim 7.5 - 9.0$ . Sun et al. (2017a,b, 2018) used upper main-sequence (UMS) stars to trace large-scale structures in major star formation complexes in the LMC and SMC. They found that the size and mass distributions follow a power law, which supports hierarchical star formation governed by turbulence. Less massive PMS stars, due to their extended PMS phase (Baraffe et al. 2015), provide valuable information about the recent star formation history (see Gouliermis 2012, for an overview). Identifying the PMS populations, including star formation sites only composed of intermediate- and low-mass stars, can thus reveal the full galaxy-wide extent of recent star formation.

We present an automated method that uses the capabilities of the VMC to detect intermediate- and low-mass ( $1 M_{\odot} \lesssim$

$M_{*} \lesssim 4 M_{\odot}$ ) PMS populations. The method is based on a colour–magnitude Hess diagram (Hess CMD) analysis, which includes corrections for reddening and completeness, in order to distinguish young populations from the field. This paper describes the development of this method as well as its application to a  $\sim 1.5 \text{ deg}^2$  region in the LMC. The chosen pilot field contains well-studied OB associations with known PMS populations that are used to calibrate and fine-tune the method. The paper is organized as follows: Sec. 2 gives an overview of the VMC survey and the data used in this work. Section 3 describes how we deal with the contamination from old field stars, while Sec. 4 explains in detail the strategy we devised to identify and categorise young populations. In Sec. 5 we present tests using synthetic and literature clusters to evaluate the sensitivity of the method for the cluster age and mass. We show in Sec. 6 first results based on the application of our method to the LMC pilot field and discuss the properties of the identified young low-mass populations. Finally, we present a summary and our main conclusions in Sec. 7.

## 2. VISTA/VMC survey data selection

The data used in this work are part of the VMC, which is an ESO public survey carried out with the VISTA InfraRed CAMERA (VIRCAM) instrument on the 4.1 m VISTA telescope (Sutherland et al. 2015). The observing strategy of the VMC involves multi-epoch imaging of tiles across the Magellanic System in the  $Y$  ( $1.02 \mu\text{m}$ ),  $J$  ( $1.25 \mu\text{m}$ ), and  $K_s$  ( $2.15 \mu\text{m}$ ) bands. One tile almost uniformly covers an area of  $\sim 1.5 \text{ deg}^2$  as a result of combining six offset paw-print images in order to fill the gaps between the 16 VIRCAM detectors. Overall, the survey consists of 110 tiles that cover an area of  $\sim 170 \text{ deg}^2$ . Upon completion, every tile will have been observed at 3 epochs in the  $Y$  and  $J$  bands, and 12 epochs in the  $K_s$  band. The exposure time per epoch is 800 s in  $Y$  and  $J$ , and 750 s in  $K_s$ , leading to total exposure times of 2400 s ( $Y, J$ ) and 9000 s ( $K_s$ ).

We chose as a pilot field the area covered by the tile LMC 7\_5. Its central coordinates are  $\alpha(\text{J2000}) \approx 81^{\circ}493$  and  $\delta(\text{J2000}) \approx -67^{\circ}895$ , which is approximately  $1^{\circ}7$  to the north-west of the Tarantula Nebula and to the north of the LMC bar. The coordinate range covered by this tile is approximately  $80^{\circ}0 \leq \alpha \leq 83^{\circ}0$  and  $-68^{\circ}6 \leq \delta \leq -67^{\circ}2$ . Figure 1 shows the location of tile LMC 7\_5 within the wider environment of the LMC. This field harbours LHA 120-N 44 and LHA 120-N 51 (Henize 1956), two large star-forming complexes (e.g. Carlson et al. 2012) that are discussed in more detail in Sec. 6.1. They include massive OB associations like LH 60 and LH 63, in which significant populations of intermediate- and low-mass PMS stars down to  $\sim 0.5 M_{\odot}$  have been identified (Gouliermis et al. 2011). Several older clusters with ages between 10 Myr and 1 Gyr are also found in this field (e.g. Glatt et al. 2010; Popescu et al. 2012).

We use a photometric catalogue obtained by performing point spread function (PSF) photometry on stacked PSF-homogenized images (Rubele et al. 2012, 2015). Previous studies have shown that PSF photometry recovers more sources in crowded regions than aperture photometry (e.g. Tatton et al. 2013). PSF photometry results in deeper and more complete catalogues especially in areas with active or very recent star formation. We tested this by comparing the PSF photometry data with aperture photometry data, reduced and calibrated with the VISTA Data Flow System (VDFS) pipeline (Irwin et al. 2004; González-Fernández et al. 2018) and retrieved from the VISTA

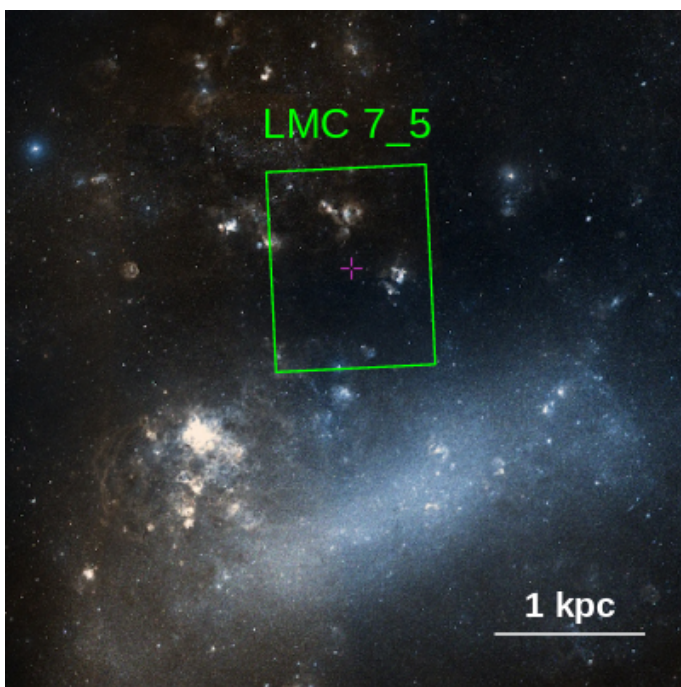


**Fig. 1.** Digitized Sky Survey (DSS) image showing the location of the pilot field (highlighted in green) within the wider LMC environment. North is up and east is to the left.

Science Archive (VSA<sup>1</sup>; Cross et al. 2012) for six circular regions with a radius of 2'. Three regions contain young OB associations (LH 54, LH 60, and LH 63), while the other three showed no sign of recent star formation activity or stellar over-densities. The PSF photometry detects  $\sim 1.4$  times more sources in regions without active star formation, and  $\sim 1.6$  times more sources in the regions containing the three young associations. In addition, the PSF catalogues provide estimates of the local completeness for every filter based on artificial star tests (Rubele et al. 2012). These estimates are used to correct for differences in the completeness between stellar populations from different regions (Sec. 3.3). For the PSF catalogue a completeness of 50% is typically reached at  $Y \approx 21.4$  mag,  $J \approx 21.3$  mag, and  $K_s \approx 20.6$  mag. The  $5\sigma$  magnitude limits are  $Y \approx 22.3$  mag,  $J \approx 21.9$  mag, and  $K_s \approx 20.9$  mag (for the nominal aperture photometry magnitude limits, see Cioni et al. 2011). Using the mean reddening in LMC 7\_5 ( $E(Y - K_s) \approx 0.18$  mag; Tatton et al., in prep.), the PSF  $5\sigma$  limits correspond to  $\sim 0.7 M_\odot$  and  $\sim 1.3 M_\odot$  for ages of 1 Myr and 10 Myr, respectively.

### 3. Constructing differential Hess diagrams

To identify young stellar populations in the pilot field, we use the star positions in the CMD, which are indicative of their masses and ages. CMD-based methods are widely used to analyse clusters of all ages (e.g. Da Rio et al. 2009; Rubele et al. 2011; Girardi et al. 2013; Niederhofer et al. 2017). In general, observations towards clusters or associations are contaminated by the dispersed field population; it is thus necessary to apply a robust decontamination procedure. In this paper we work with  $K_s/(Y - K_s)$  CMDs, since the longer wavelength baseline makes different populations easier to distinguish.

#### 3.1. CMD density diagrams

We start by spatially dividing the pilot field into a grid (see Fig. 2). Every grid element is circular, and the distance between the centres of two neighbouring elements is one grid element radius. The resulting overlap ensures that every location is covered by the grid. It also reduces the chance that a young cluster or association is split up between two or more neighbouring grid elements. The grid radius is a very important parameter, and it is the subject of extensive testing in this study (see Sec. 5). We defined grids with radii of  $r = \{90'', 75'', 60'', 50'', 40''\}$ . Individual  $K_s/(Y - K_s)$  CMDs are constructed for each grid element. The CMDs are then smoothed using a Gaussian kernel, resulting in a 2D density map of the stellar distribution in colour–magnitude space. The widths of the kernels define the colour–magnitude resolution of our density maps; they must be small enough to highlight the distribution of different stellar populations in the CMD, but large enough to be robust against small number statistics. We apply an adaptive kernel width that depends on the number of stars in a grid element ( $N_{*,ge}$ ) and on the photometric errors as follows:

$$\sigma_{K_s} = 0.2 \text{ mag} \times \sqrt{\frac{\langle N_* \rangle}{N_{*,ge}}} \quad (1)$$

$$\sigma_{Y-K_s} = 0.5 \times \sigma_{K_s}, \quad (2)$$

where  $\langle N_* \rangle$  is the median number of stars in the coarsest grid. If the mean photometric error within the kernel,  $\Delta K_s > \sigma_{K_s}$  we adopt  $\sigma_{K_s} = \Delta K_s$ . The width values are typically in the ranges  $0.1 \text{ mag} < \sigma_{Y-K_s} < 0.2 \text{ mag}$  and  $0.2 \text{ mag} < \sigma_{K_s} < 0.4 \text{ mag}$ . Kernel width maxima of  $\sigma_{Y-K_s} = 0.2 \text{ mag}$  and  $\sigma_{K_s} = 0.4 \text{ mag}$  are set to prevent smoothing over too large CMD regions. The smoothing procedure results in a Hess CMD for every grid element. Figure 3 shows representative CMDs (top) and Hess CMDs (bottom) for two grid elements containing mostly old field stars (left) and a star-forming region (right), as shown by the overplotted PARSEC<sup>2</sup> isochrones (Bressan et al. 2012).

#### 3.2. Control field selection

To decontaminate each grid element from field stars, we use offset control fields that closely resemble the local field population. The total size of the pilot field precludes the use of a single control field for the whole tile, since the typical field population changes over such large spatial scales. Hence it is necessary to define control fields individually for every grid element. The approach is as follows: we count stars within the UMS and PMS regions of the CMD (shown in Fig. 3) for all grid elements within a distance of 1000'' from the grid element being analysed. The UMS and PMS regions are defined primarily using PARSEC isochrones. Furthermore, the red limit for the PMS region excludes background galaxies (Kerber et al. 2009), while the blue edge excludes most old field stars. The boundary at bright magnitudes is generous enough to allow for effects like PMS variability and IR excesses, and the lower boundary is imposed by the sensitivity of the survey. The CMD of a typical LMC field population is expected to have significantly fewer stars within the UMS and PMS regions than that of an area dominated by young stars. Star counts can thus identify grid elements that are control field candidates. An example control field search area is depicted in Fig. 2. The number of grid elements within this area

<sup>2</sup> PAdova and TRieste Stellar Evolution Code  
[http://stev.oapd.inaf.it/cgi-bin/cmd\\_2.7](http://stev.oapd.inaf.it/cgi-bin/cmd_2.7)

<sup>1</sup> <http://horus.roe.ac.uk/vsa/>

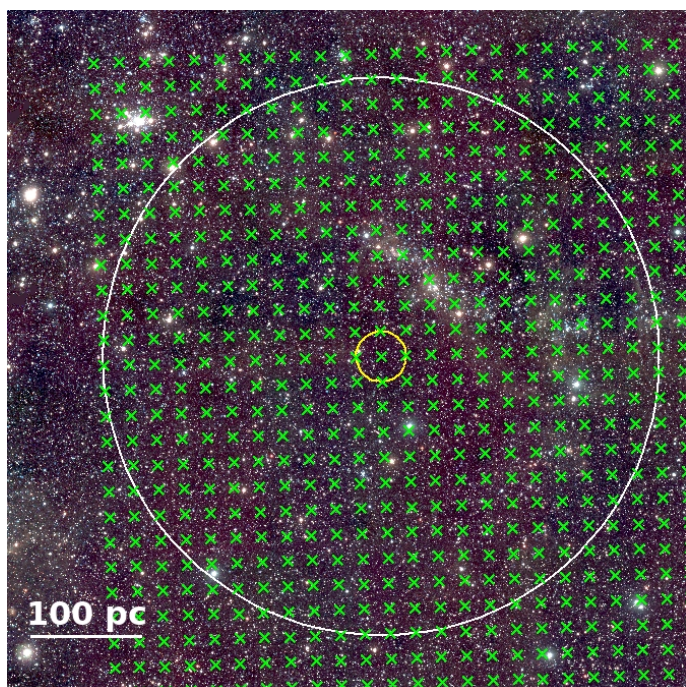


**Fig. 2.** VISTA RGB composite with  $Y$  ( $1.02 \mu\text{m}$ ) in blue,  $J$  ( $1.25 \mu\text{m}$ ) in green, and  $K_s$  ( $2.15 \mu\text{m}$ ) in red showing the north-eastern corner of the pilot field. Green crosses are placed at the centres of the grid elements ( $90''$  radius in this instance). The small yellow circle highlights an example grid element, while the large white circle shows the area searched to identify suitable control field regions (see text).

varies, depending on the size of the elements; the coarsest grid ( $90''$  radius) contains around 360 grid elements. We create histograms of the star counts for both the UMS and PMS regions and approximate these with Gaussian distributions.

In addition, the mean extinction towards every grid element within the control field search area is determined by using the mean observed colour of red clump (RC) stars. These are evolved stars with well-constrained luminosities, and thus the RC is often used for distance and reddening measurements (e.g. Paczyński & Stanek 1998; Tatton et al. 2013). Although population effects change the absolute magnitude of RC stars (Girardi & Salaris 2001), any variations on  $\ll$  kpc scales are generally dominated by distance differences and reddening. The selection box for the RC is also indicated in Fig. 3. Its slope of 0.434 is calculated based on the relative extinctions for VISTA filters,  $A_Y/A_V \approx 0.390$  and  $A_{K_s}/A_V \approx 0.118$  (Catelan et al. 2011). The  $Y - K_s$  colour limits were chosen to keep the contamination by non-RC objects low, while still covering typical LMC reddening values (Rubele et al. 2012; Tatton et al. 2013). Assuming an intrinsic RC colour of  $(Y - K_s)_0 = 0.84$  mag (Tatton et al. 2013), we probe extinction values up to  $A_V \approx 4.26$  mag. The magnitude limits are such as to be insensitive to the small distance variations due to the depth of the LMC along the line of sight. We create a histogram of all mean extinction values within the control field search area, and fit it with a Gaussian distribution. Across the pilot field, the mean extinction is  $A_V \approx 0.7$  mag, consistent with another determination using the RC method ( $A_V \approx 0.66$  mag; Tatton et al. in prep.).

A grid element is considered a reliable control field candidate if its UMS and PMS counts, and mean extinction are within  $1\sigma$  from the mean value of the respective Gaussian distributions. Usually, over 100 suitable control field candidates are found within any given  $1000''$  search area (61 is the minimum). The

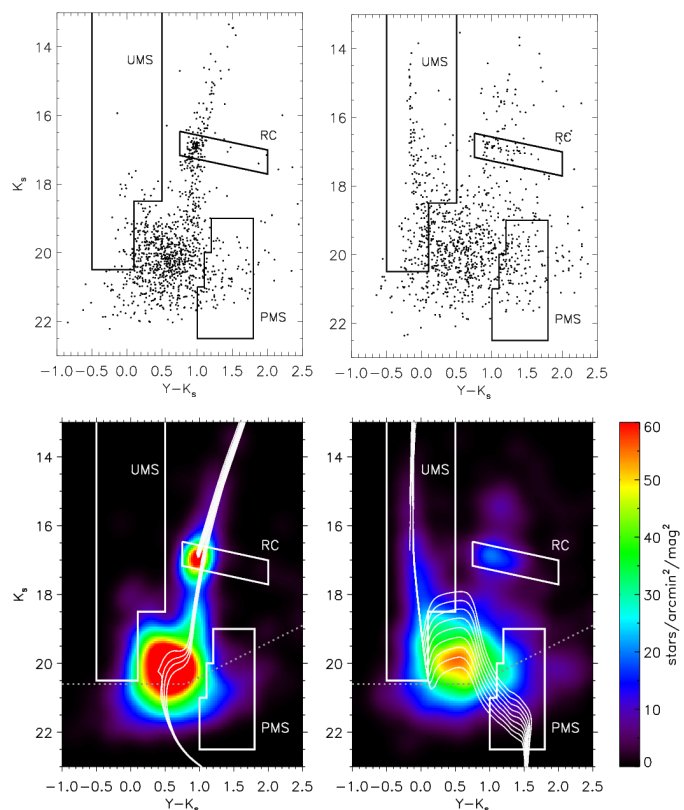


**Fig. 3. Top:** CMDs of two example grid elements. Boxes indicate the UMS and PMS regions used in the control field selection, as well as the RC region used to determine the mean extinction (see Sec. 3.2 for details). The slope of the RC selection box is defined by the reddening vector. **Bottom:** Corresponding Hess CMDs. Thin solid lines are PARSEC isochrones (Bressan et al. 2012) for  $\log(t/\text{yr}) \in [9.5, 9.6, 9.7, 9.8]$  and  $Z = 0.0033$  (left panel), and  $\log(t/\text{yr}) \in [6.0, 6.1, 6.2, 6.3, 6.4, 6.5, 6.6, 6.7, 6.8]$  and  $Z = 0.008$  (right panel). The assumed metallicities are typical for the age ranges (Rubele et al. 2012; Tatton et al. 2013). The isochrones are shifted by a distance modulus of 18.49 mag (de Grijs et al. 2014), and an extinction correction derived from the RC analysis (see text) is applied. The dotted line marks the typical 50% completeness level.

algorithm automatically selects the  $N$  nearest control field candidates and combines them into a master control field. The chosen value for  $N$  depends on the grid radius:  $N = 10, 14, 20, 28,$  and  $40$  for the  $90'', 75'', 60'', 50'',$  and  $40''$  grids, respectively. These values provide a good balance between computing time and well-sampled control field populations.

### 3.3. CMD residuals and significance maps

In order to compare the stellar content of a grid element to that of the respective master control field, it is necessary to correct for differences in the reddening, since reddened main-sequence stars can occupy the same region in the CMD as PMS stars. Using the mean extinction values determined in Sect. 3.2 is not appropriate since it would not account for differential reddening. Instead, the magnitudes of the stars in the control fields are individually corrected. We start by determining the cumulative colour distribution of stars in the RC box (as defined in Sec. 3.2) for each grid element and the corresponding master control field (Fig. B.1). For every control field star a random number is generated. This number is taken as a percentile in the cumulative distributions of the RC stars; each star is in turn dereddened by the corre-

sponding  $E(Y - K_s)$  in the colour distribution of the control field, and subsequently reddened by the corresponding  $E(Y - K_s)$  in the colour distribution of the grid element. By shifting all stars from the control field along the reddening vector so that both RC colour distributions closely match each other (Fig. B.1), any reddening differences between the grid element and its control field are minimised. More details on this procedure can be found in Appendix B.

Since the reddening procedure shifts control field stars to fainter magnitudes and redder colours, its completeness values need to be adjusted. Even if the areas considered display similar extinction levels, there can be differences in the completeness due to crowding. We compare the original catalogue completeness of each control field star to the average completeness of stars located in the vicinity of its shifted CMD position (in the grid element being studied). Control field stars are assigned a weight equal to the ratio of the original and shifted completenesses. Weights smaller than unity lead to lower densities in the Hess diagram, simulating the fact that fewer stars would have been detected.

A Hess CMD is generated for the reddened master control field in a similar way as for the corresponding grid element (Sec. 3.1), but using a convolution of completeness weights and Gaussian kernel in the smoothing process. Finally, the Hess CMD of the reddened control field is subtracted from that of the grid element analysed. The result is a differential Hess CMD (henceforth residual map) in which differences between specific stellar populations and the local field population stand out as density excesses (examples in the top panels of Fig. 4).

We use Poisson statistics to obtain the significance of any density excesses in the residual maps. If  $n_{ge}$  and  $n_{cf}$  are the density values at a specific location in the Hess diagram for the grid element and the control field, respectively, then the density excess is simply  $n_{ge} - n_{cf}$ ; the individual statistical uncertainties are  $\sqrt{n_{ge}}$  and  $\sqrt{n_{cf}}$ , which gives a total uncertainty of  $\sqrt{n_{ge} + n_{cf}}$  for the residual. The statistical significance in the residual is thus

$$\sigma_{\text{residual}} = \frac{n_{ge} - n_{cf}}{\sqrt{n_{ge} + n_{cf}}}. \quad (3)$$

This significance is computed for every point in the residual map, creating an associated significance map. Figure 4 (bottom panel) shows an example significance map. We apply the algorithm to the five grids with different radii; for every element in each grid a residual map and a significance map are obtained.

#### 4. Identifying candidate young regions

We developed a procedure that analyses the residual and significance maps, flagging and categorising candidate regions. This was extensively tested by comparing the significance maps from grid elements containing the well-studied associations LH 60 and LH 63, and a nearby control field (Gouliermis et al. 2011). Figure 4 (top) shows residuals for the control field (left) and a grid element that contains LH 63 (right). The bottom panel shows the significance map that results from applying Eq. 3 to the LH 63 residual. It displays extended areas with significances  $> 2$  at CMD locations that are indicative of the presence of young UMS and PMS stars.

A prominent blue patch is also noticeable, suggesting a field over-subtraction, where one would expect faint main-sequence stars. This feature is likely caused by small-scale variations in the completeness that are due to crowding, which are not accurately accounted for in our method. The dark blue areas at the

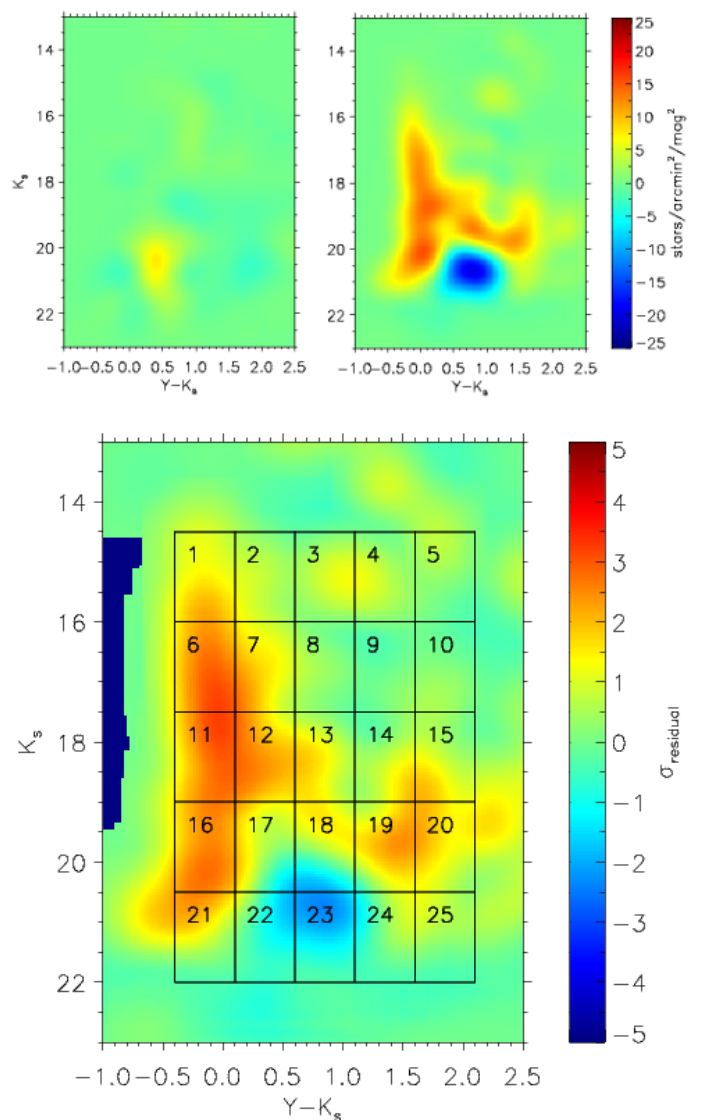


**Fig. 4.** **Top left:** Residual map generated for a grid element showing no significant density excesses, leading to a featureless residual map; such a grid element is thus dominated by the old LMC field population. **Top right:** Residual map for a grid element that includes the OB association LH 63. Significant density excesses can be seen across the CMD, which is due to the presence of massive OB and PMS stars. **Bottom:** Significance map for the same LH 63 region with 25 CMD boxes overlaid; these are used to classify candidate regions based on observed density excesses (see Sec. 4).

edge of the map are artefacts caused by the absence of stars at these CMD positions for the grid element and the corresponding control field.

We divide the colour–magnitude space into 25 boxes (Fig. 4 bottom panel), which are analysed separately. A box is flagged when the average statistical significance is higher than a predefined threshold. The threshold value is chosen to balance sensitivity to less populous associations and robustness against statistical fluctuations. To find an appropriate threshold, we analyse the distribution of the average significances in all CMD boxes across the whole tile. This distribution is approximated by a Gaussian, and the width  $\sigma$  describes the typical statistical fluctuation. We use either  $2.5\sigma$  or  $3\sigma$  as the flagging threshold (details to follow).

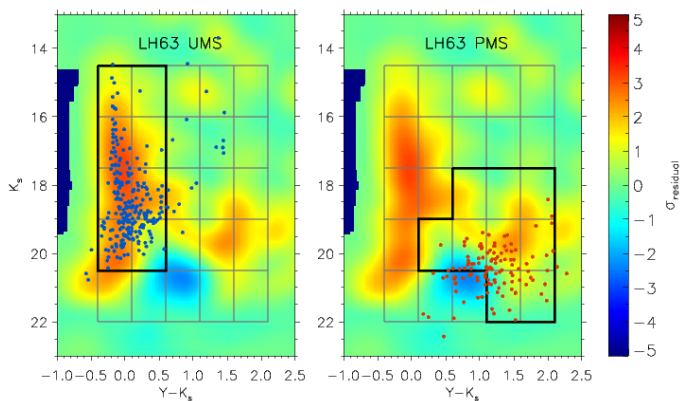


**Fig. 5.** Same significance map in the background as shown in Fig. 4 (bottom). Blue and red symbols display VMC sources that are successfully matched to the LH 63 UMS (left) and PMS (right) catalogues from Gouliermis et al. (2011). Thick black lines highlight the boxes relevant for the UMS and PMS classifications, respectively (see also Fig. 6).

Depending on their properties (i.e. age and total mass), stellar populations create density excesses above the local field population in different areas of the significance maps. We analysed the residuals and significance maps for example regions with known young populations. Gouliermis et al. (2011) constructed catalogues of candidate PMS and UMS stars for LH 60 and LH 63 (age 3 – 5 Myr), based on a statistical analysis of HST photometry in the  $F555W$  and  $F814W$  filters. After correcting for a systematic difference of  $0.42''$  in RA, we cross-correlated the HST and VMC catalogues with a conservative  $0.3''$  matching radius. We further compared the magnitudes of the matched pairs in the VISTA  $Y$  filter and in the HST  $F814W$  filter. The transmission curves of these filters are similar enough for these magnitudes to be comparable. For the matched pairs ( $F814W - Y$ ) is on average 0.43 mag, with a dispersion of 0.86 mag. To select a clean sample, pairs with  $(F814W - Y) \geq 2$  mag were excluded.

In LH 60 we found 112 and 174 VMC counterparts to the HST PMS and the UMS sources, respectively. For LH 63 the corresponding numbers are 125 and 269<sup>3</sup>. Figure 5 shows the VMC counterparts for the LH 63 UMS and PMS catalogues, with the significance map shown in the background. A clear gap is visible between the two populations, since the HST catalogue excludes areas in the optical CMD that are heavily contaminated by field stars. Clearly, the UMS matches coincide very well with areas of statistically significant density excesses; the highlighted CMD boxes (Fig. 5 left) cover the majority of UMS matches and the corresponding density excesses. Overall, 237 out of 269 UMS matches are located within these eight boxes; some matches are located near the red giant branch and are likely contaminants in the UMS catalogue (Gouliermis et al. 2011).

The situation is more complicated for the PMS matches. Some matches fall on the strong negative density excess described previously; we did not use this part of the CMD to identify PMS populations precisely to avoid severe contamination by main-sequence stars. The large scatter in the CMD distribution of the PMS matches can be due to photometric errors and/or young stellar variability (e.g. T Tauri stars or FU Orionis variables; Contreras Peña et al. 2014; Rice et al. 2015). In addition, the PMS population could have either an age spread, or it could consist of multiple populations with different ages, similar to

<sup>3</sup> Based on a catalogue matching with shifted coordinates, we estimate that  $\sim 3\%$  of the UMS matches and  $\sim 10\%$  of the PMS matches are spurious.

what has been seen in Orion (Beccari et al. 2017). Nevertheless, the regions with the most significant density excesses suggest a PMS distribution that is brighter than the distribution of HST-matched stars. Two effects likely contribute to this. Firstly, small-scale completeness variations can be significant in crowded regions like LH 63 (see Sec. 3.3). This can lead to over-subtraction during the control field decontamination process, which eliminates a potential density excess due to faint PMS stars. Secondly, the HST PMS catalogue included mostly relatively faint PMS stars ( $F814W \geq 21.2$  mag). The density excess seen in our maps includes brighter PMS candidates excluded from HST optical catalogues. Using the location of the PMS matches and the location of the typical density excesses seen in the residual maps of known young associations, we selected the CMD boxes highlighted in the right panel of Fig. 5 as PMS indicators. Ninety-six out of 125 PMS matches are within this area, and overall, around 85% of the HST–VMC counterparts are located within the outlined UMS and PMS boxes.

Using these contiguous regions in the CMD that are indicative of the presence of specific populations, we classify each grid element based on which boxes are flagged in its significance map. Four classifications are adopted:

1. **UMS-only:** At least two adjacent boxes are flagged in the UMS CMD region. Figure 6 (left) shows a typical example of this classification. It covers a broad age range from  $\sim 10$  to  $\sim 300$  Myr. Based on artificial cluster tests (see Sec. 5.1), a minimum cluster mass of  $\sim 500 M_{\odot}$  is needed to reliably flag two UMS boxes. For populations younger than 10 Myr, the PMS population is also detectable, changing its classification to UMS+PMS (see below). Beyond  $\sim 300$  Myr, sufficiently massive clusters ( $> 1000 M_{\odot}$ ) create a significant red giant excess, which will trigger the classification “old”.
2. **PMS-only:** At least two adjacent boxes are flagged in the PMS CMD region (second panel in Fig. 6). This classification traces young ( $< 10$  Myr), low-mass clusters and associations up to around  $\sim 500 M_{\odot}$ . While the PMS phase for stars with masses  $\lesssim 0.5 M_{\odot}$  can last up to 100 Myr (e.g. Tout et al. 1999), PMS populations older than  $\sim 10$  Myr are too faint to be detected in the VMC survey. Young clusters and associations with masses above  $500 M_{\odot}$  also flag boxes typical of UMS populations, changing the classification to UMS+PMS.
3. **UMS+PMS:** A grid element is classified as UMS+PMS if a total of at least three boxes in both the typical PMS and UMS CMD regions are flagged. Adjacency is not strictly enforced, since a minimum of three flagged boxes always leads to reasonable combinations. The same age range as in the PMS classification is probed ( $< 10$  Myr), but the clusters and associations are more massive, since enough massive stars need to be present to flag UMS boxes. Examples for this classification are shown in Fig. 6 (third panel) and Fig. 4.
4. **Old:** This classification requires a minimum of three flagged boxes in the red giant branch and the fainter parts of the UMS CMD region. The flagging threshold for the red giant branch boxes is  $2.5\sigma$  (compared to  $3\sigma$  for the other boxes). We found in tests with synthetic and real clusters that this threshold reduction improves our ability to classify old clusters, without a noticeable increase in the number of false positives. Grid elements with clusters older than  $\sim 300$  Myr and more massive than  $\sim 1000 M_{\odot}$  fall into this classification (Fig. 6, right).

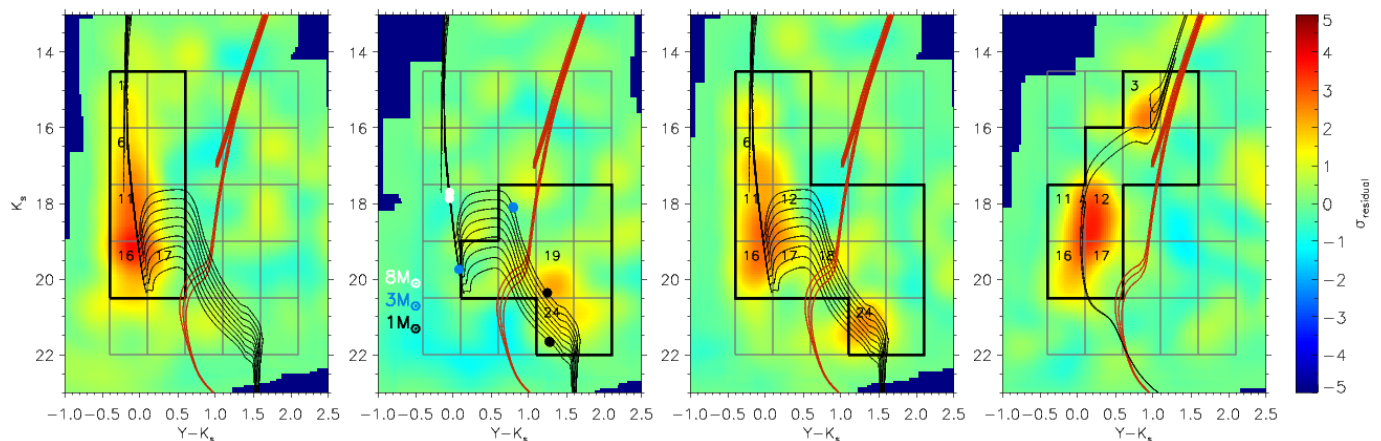


**Fig. 6. From left to right:** Significance maps for grid elements classified as UMS-only, PMS-only, UMS+PMS, and “old”. The CMD boxes relevant for each classification are highlighted. Boxes that are flagged in the particular significance map are numbered. PARSEC isochrones (Bressan et al. 2012) are shown in all panels. Red isochrones represent ages from  $\log(t/\text{yr}) = 9.6$  to  $9.8$ , with a metallicity of  $Z = 0.0033$  (Tatton et al. 2013); they show the typical location of the old LMC field population. Black isochrones represent young populations from  $\log(t/\text{yr}) = 6.0$  to  $6.8$  ( $Z = 0.008$ ; Rubele et al. 2012). The two black isochrones in the rightmost panel represent populations of  $\log(t/\text{yr}) = 8.5$  and  $8.6$  ( $Z = 0.008$ ). All isochrones are reddened according to the mean extinction for that particular grid element (Sect. 3.2). In the second panel the theoretical positions for stars of three different masses are shown (colour-coded circles) for the youngest and oldest black isochrones.

## 5. Testing the identification strategy

### 5.1. Synthetic clusters

To assess the sensitivity of this procedure to young populations of different masses and ages, we ran tests using synthetic clusters. To generate the synthetic clusters, we used the Popstar Evolutionary Synthesis Code (Mollá et al. 2009) and adopted a Kroupa IMF (Kroupa 2001, 2002). There is no conclusive evidence that the IMF in the LMC is significantly different from the Galactic IMF (for  $M > 1 M_{\odot}$ ; Gruendl & Chu 2009; Liu et al. 2009a,b), with the possible exception of 30 Doradus (Schneider et al. 2018b). NIR photometry for the VISTA filter set was obtained using PARSEC models (Bressan et al. 2012). Synthetic clusters were generated for the following mass and age combinations:

- $M_{\text{cl}} \in [250 M_{\odot}, 500 M_{\odot}, 1000 M_{\odot}, 2000 M_{\odot}, 3000 M_{\odot}]$
- $\log(t/\text{yr}) \in [6.0, 6.3, 6.7, 7.0, 7.5, 8.0, 8.5, 9.0]$ .

The cluster masses are representative of LMC clusters within this age range (de Grijs & Anders 2006). We also adopted the canonical LMC metallicity of  $Z = 0.008$ . For every mass–age combination, ten clusters were created. Incompleteness was applied and photometric errors added to match the quality of the VMC data before injecting the clusters into the PSF tile catalogue. All clusters were seeded in control-field-like grid elements with flat significance maps. Each synthetic cluster was fully contained within a grid element, a reasonable assumption given that even the smallest elements have a physical radius of 10 pc ( $1 \text{ pc} \cong 4''$  at the LMC distance). The enhanced PSF tile catalogues for every synthetic cluster were ingested into our algorithm, and the resulting residuals and significance maps were evaluated. If a synthetic cluster was classified into one of the four classes defined in Sec. 4 and in agreement with the cluster input properties, it is considered to be reliably identified.

In Fig. 7 we show examples of significance maps generated from observed data, compared with maps generated from synthetic clusters. The top left panel shows a PMS-only classified element with a clear PMS signal and no UMS excess. This suggests the presence of a very young, low-mass population. A synthetic population of  $250 M_{\odot}$  with an age of 1 Myr generates a

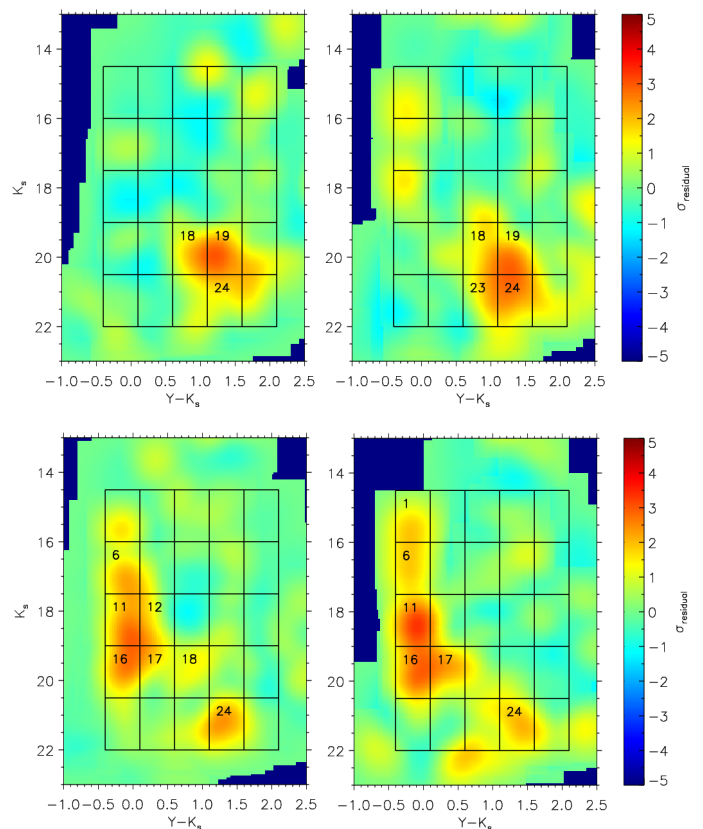


**Fig. 7. Top:** Significance map for a PMS-only classified grid element (left) is compared to a synthetic stellar population of  $250 M_{\odot}$  and 1 Myr (right). **Bottom:** Similar to the top, but showing a UMS+PMS classified grid element (left) and a synthetic stellar population of  $1000 M_{\odot}$  and 5 Myr (right). Flagged boxes are numbered in each map.

very similar significance map. The bottom left panel contains the significance map for a UMS+PMS classified element. A synthetic stellar population of  $1000 M_{\odot}$  with an age of 5 Myr creates a similar significance map. Since at 5 Myr many PMS stars fall below the sensitivity limit, the PMS signature is relatively weak.

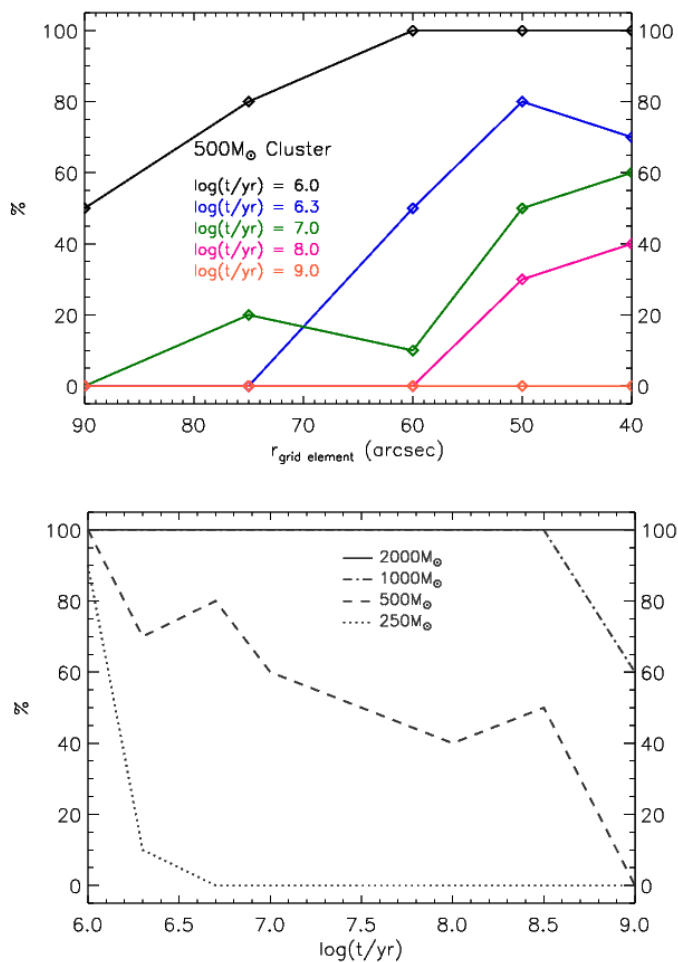


**Fig. 8. Top panel:** Detection percentages for  $500 M_{\odot}$  clusters of different ages for grid-element radii from  $90''$  to  $40''$ . A general increase in detection rates with decreasing radius is noticeable. A decrease in detection rates with increasing cluster age is evident as well. **Bottom panel:** Detection percentages for clusters of four different masses across the age range from 1 Myr to 1 Gyr for the  $40''$  radius. A decrease in sensitivity for older ages and lower masses is apparent. Clusters more massive than  $500 M_{\odot}$  show high detection rates for young ages.

Fig. 8 shows the results of our synthetic cluster tests. In the top panel the detection rates for the different grid element radii for  $500 M_{\odot}$  clusters of various ages are presented. While for the  $90''$  radius clusters of this mass are rarely detected, the percentages increase steadily for smaller radii. At a radius of  $40''$  the detection rates are at least 60% for ages where one would expect to find PMS stars. The bottom panel shows the results obtained using the  $40''$  grid for four different cluster masses in more detail. For masses  $\geq 1000 M_{\odot}$ , clusters are always detected, with a drop in detection rate only noticeable at 1 Gyr. For lower masses, the detection rate drops steadily with age. This is due to a decrease of flagged UMS boxes with increasing age, as more massive stars evolve away from the main sequence onto the red giant branch. At these cluster masses, this does not necessarily trigger the flagging of boxes that lead to the “old” classification. For ages  $\lesssim 10$  Myr, the majority of  $500 M_{\odot}$  clusters are detected. Even though the detection rate drops sharply for masses  $< 500 M_{\odot}$ , it remains high for very young ages.

These tests reveal three clear trends. Rather obviously, the more massive a synthetic cluster at any given age, the higher the probability of a reliable detection. Secondly, with smaller

grid element radius, the probability of detection for a given synthetic cluster mass and age increases. The reason is that the same number of synthetic stars cause a higher density excess in the residuals of smaller grid elements, leading to a higher flagging probability. Thirdly, the detection rates generally decrease with age. The luminosity of intermediate- and low-mass PMS stars decreases as they approach the main sequence. Hence, an increasing fraction of PMS stars falls below the sensitivity limit of the VMC survey for progressively older ages.

Table 1 presents an overview of the most common classifications for synthetic clusters of different age and mass ranges. The decrease of detectable PMS stars with age causes an increase in the minimum cluster mass that is necessary to detect a PMS signature. Beyond 10 Myr, the VMC survey is not sufficiently deep to reliably detect any remaining PMS stars. Therefore, all detected clusters are classified either as UMS-only or as “old”. The tests reveal that massive ( $\geq 2000 M_{\odot}$ ) clusters within the age range 30 Myr – 1 Gyr can be mis-classified as UMS+PMS, and thus contaminate the UMS+PMS class. However, the level of contamination is 2.5% at most.

In summary, we conclude that for a given mass, a cluster or association is easier to detect and classify at a young age (preferably  $< 10$  Myr); this is mostly due to the sensitivity and completeness limits of the VMC survey. While  $\sim 28\%$  of detected clusters with age 10 Myr have a PMS signature leading to a PMS-only or UMS+PMS classification, this fraction increases to  $\sim 66\%$  for 5 Myr-old populations and  $\sim 98\%$  for very young ages ( $\leq 2$  Myr). More massive clusters are obviously more likely to be identified. Another important result is that finer grids are better suited to finding low-mass clusters, despite the effects of small number statistics due to the decreasing number of stars per grid element.

## 5.2. Literature clusters

The synthetic cluster tests provided valuable results about the mass and age ranges that are effectively traced with our method. However, as these synthetic clusters were only injected into the PSF catalogue rather than into the images, information on the sensitivity to different cluster radii and star count density profiles is lacking. We compiled a list of 31 clusters and associations from the literature (Gouliermis et al. 2003; Glatt et al. 2010; Popescu et al. 2012). Our list is not a complete census of clusters in the pilot field, but provides a reliable sample of clusters with different ages and sizes. The selected systems span an age range from a few Myr up to around 1 Gyr, and apparent sizes from  $10''$  to over  $100''$  (sizes were estimated visually from the VMC images).

Table 2 shows how many clusters are classified as a function of grid element radius. With decreasing grid element size, the number of unclassified clusters decreases monotonically. This trend is in line with the results from the synthetic cluster tests, where an increasing sensitivity for the finer grids was observed. For the finest grid, 25 out of 31 literature clusters are classified with our method. For 23 of these, their classifications and inferred broad age range (see Table 1) are consistent with published literature ages. The two remaining clusters have literature ages of  $\log(t/\text{yr}) \sim 7.8$ ; since an RC signature is detected, our method classifies these clusters as old, implying an age  $\geq 300$  Myr.

Six unclassified clusters remain, four of which flag a single CMD box. Since this does not trigger a classification, these four clusters are at the sensitivity limit of the  $40''$  grid. The unclassified clusters are either spatially small compared with the



**Table 1.** Most likely classifications for mass and age ranges based on synthetic cluster tests.

	< 2 Myr	2 – 5 Myr	5 – 10 Myr	10 – 300 Myr	> 300 Myr
< 500 $M_{\odot}$	PMS-only	-	-	-	-
500 – 1000 $M_{\odot}$	UMS+PMS	UMS+PMS	UMS-only	UMS-only	UMS-only
> 1000 $M_{\odot}$	UMS+PMS	UMS+PMS	UMS+PMS	UMS-only	old

**Table 2.** Number of classified clusters from the sample of 31 clusters from the literature as a function of grid element radius.

	90''	75''	60''	50''	40''
classified	20	23	23	24	25
unclassified	11	8	8	7	6

grid element and/or are relatively old (based on their literature ages). Two of the six unclassified clusters are the smallest in our list with radii of 10'' and 14'',  $\sim 6\%$  and  $\sim 12\%$  of a grid element area. This indicates that our method is mostly sensitive to clusters with  $r \gtrsim 3$  pc at the LMC distance. For four of the six unclassified clusters, the literature age is in the range  $7.3 \lesssim \log(t/\text{yr}) \lesssim 8.7$ . The stellar populations of old clusters move towards areas in the CMD that are more heavily contaminated by the old field population, further decreasing the sensitivity. This confirms the results from the synthetic cluster tests that comparatively old systems have lower detection rates. Given that our stated goal is to identify young populations, a decrease of detection rate with cluster age is not an issue.

### 5.3. Final choice of grid element radius

Our analysis clearly advocates the use of the 40'' radius grid because of its increased sensitivity. A further decrease in radius leads to grid elements without any RC stars, impairing the ability of the method to correct for reddening differences between a grid element and its control field. On average, a 40'' grid element is populated by 265 stars, with 171 stars being the minimum. Our subsequent analysis focuses on the optimal 40'' radius grid.

## 6. Results

Applying our method to the PSF catalogue from the pilot field provides the residual and significance maps, flagged boxes, and classification for every grid element. For the 40'' grid, 10,730 grid elements are unclassified, 298 are classified as UMS-only, 84 as PMS-only, 124 as UMS+PMS, and finally, 14 are classified as “old”.

### 6.1. Spatial distribution of the young populations

#### 6.1.1. Global properties

Figure 9 shows the spatial distribution of the 208 grid elements with a significant PMS contribution (classified as UMS+PMS and PMS-only, cyan and yellow crosses, respectively). These grid elements are not distributed uniformly, but instead concentrate in areas with enhanced dust emission as traced by *Spitzer* in the IRAC 8.0  $\mu\text{m}$  band (Meixner et al. 2006). Around 80% of them are found in three main regions: N 44, N 51, and N 148 (see Fig. C.1 for a detailed view). N 44 and N 51 are well-studied large star formation complexes (e.g. Carlson et al. 2012). Almost all classified elements associated with these complexes are located within regions of about 290 arcmin<sup>2</sup> ( $\sim 65,200$  pc<sup>2</sup>) and

380 arcmin<sup>2</sup> ( $\sim 85,500$  pc<sup>2</sup>). On these spatial scales, star formation complexes contain young populations formed in multiple and/or extended star formation events (see Gouliermis 2018, for a detailed review). For comparison, the HTTP survey of the 30 Doradus region covers  $\sim 168$  arcmin<sup>2</sup> (Sabbi et al. 2013), within which Schneider et al. (2018a) found evidence for complex spatial and temporal substructure amongst the massive stars. Towards the south-eastern corner of the field lies another concentration of classified elements associated with N 148, which is also prominent in CO (Wong et al. 2011) and dust emission (Meixner et al. 2006). A fourth group is situated to the north-east (labelled Region A). While the numbers of PMS-only and UMS+PMS classified grid elements are small, this region exhibits the highest concentration of UMS-only classified elements (see Appendix A), indicating a comparatively mature population. Another concentration of classified elements is associated with the emission nebula N 138. A more detailed discussion of these individual regions is found in Sec. 6.1.2.

Outside these complexes, classified grid elements are fairly scattered; Fig. 9 shows 12 isolated elements with signatures of a young population. An inspection of the residuals and significance maps for these isolated elements shows that they are generally consistent with the maps from elements located within star-forming complexes and from the synthetic clusters. A comprehensive analysis of the stellar populations of these isolated elements is beyond the scope of this paper.

Overall, UMS+PMS classified grid elements are almost exclusively found in groups. PMS-only grid elements, on the other hand, are often located on the outskirts of populous UMS+PMS star groups or appear isolated. To quantify the degree of clustering, we calculated the distance between every possible pair of classified elements. Figure 10 (top) shows this distance distribution, together with a distribution for a same-size sample of randomly placed unclassified elements. To eliminate statistical fluctuations, we ran this simulation 100 times and used the mean and standard deviation values to construct the random distribution histogram with corresponding uncertainties. Because of the finite pilot field size, the number of possible random pairs decreases for large distances. For small distances ( $< 180$  pc), the observed distribution shows a clear excess of classified pairs as a consequence of the clustered distribution of young stars. The broad peak between 450 pc and 700 pc is due to the distances between N51 and N44, and between N51 and Region A. The peak between 900 pc and 1050 pc is caused by the distances between N44 and N 148, N44 and Region A, and N51 and N 148.

Figure 10 (bottom) displays the distance distribution for the PMS-only and UMS+PMS subsamples separately. They are distinct and not simply scaled-down from the overall distribution. As a result of the very strong clustering of the UMS+PMS classified elements, the corresponding distribution shows very prominent peaks. The very narrow peak between  $\sim 130$  pc and  $\sim 170$  pc is due to the distances between associations within N44 and N51. The broad peak for distances  $\lesssim 200$  pc suggests a similar distribution of UMS structure sizes, as seen in other star formation complexes in the LMC (Sun et al. 2017b,a) and in the SMC (Sun et al. 2018).

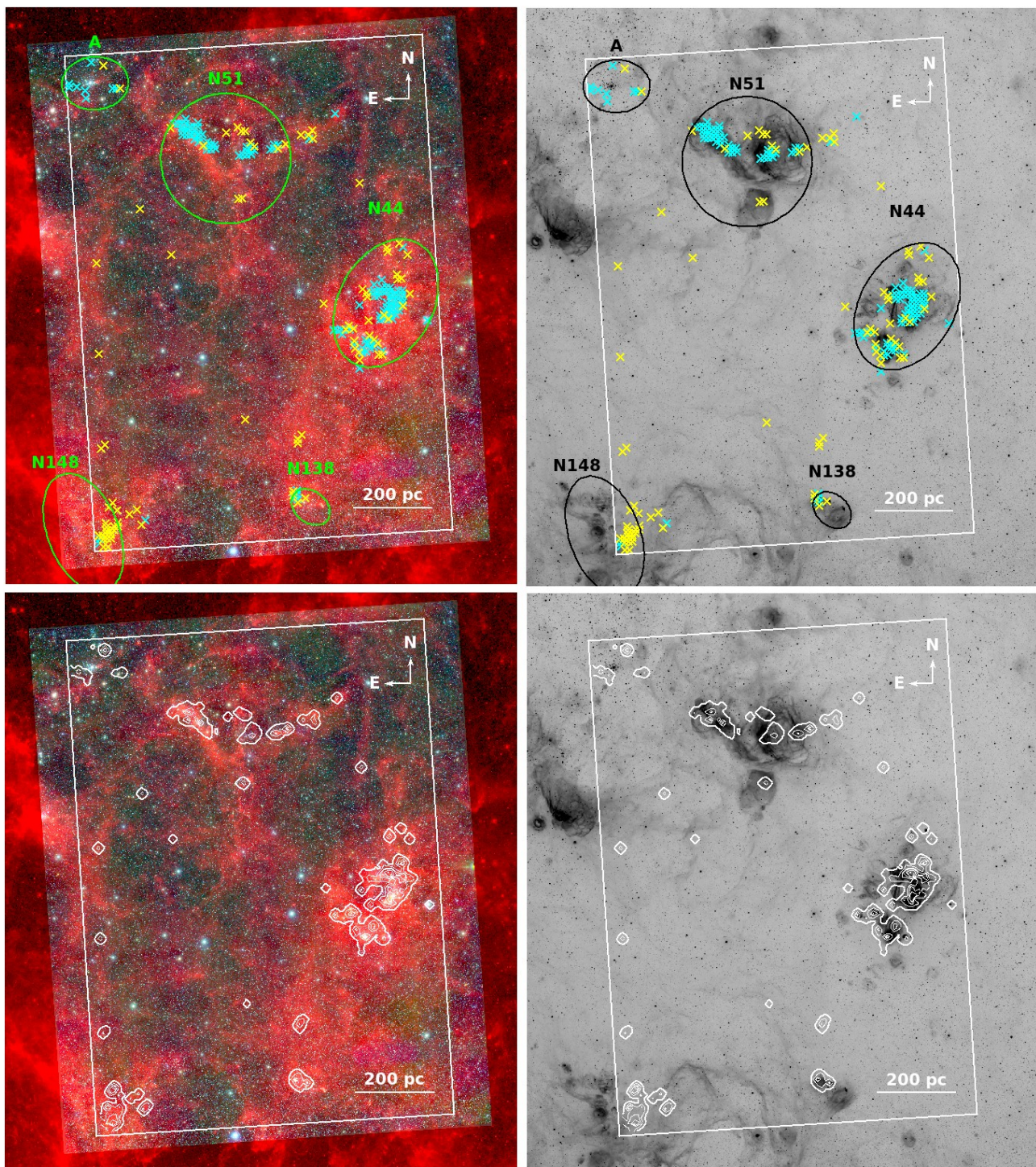


**Fig. 9.** **Top left:** Three-colour composite image with VMC  $Y$  (blue) and  $K_s$  bands (green), and *Spitzer* IRAC  $8.0\mu\text{m}$  (red). The rectangle shows the region covered by our analysis. Small crosses mark the centres of grid elements for the  $40''$  grid that are classified as PMS-only (yellow) or UMS+PMS (cyan). Several prominent regions are highlighted and labelled (spatial sizes according to Bica et al. 2008) and discussed further in Sec. 6. **Top right:** Inverted grey-scale map of  $H\alpha$  emission (Smith et al. 2005). **Bottom:** PMS density contours for elements classified as PMS-only or UMS+PMS derived from the residual maps of the grid elements. The outermost contour represents  $\Delta n_{\text{PMS}} = 2.4 \text{ stars arcmin}^{-2}$  (see Sec. 6.2 for details); every subsequent contour represents an increase in density by  $3 \times \Delta n_{\text{PMS}}$ .

In contrast, the PMS-only distribution shows smaller variations, in agreement with a more extended spatial distribution. It is a common observation in young clusters that high-mass stars are more centrally located than intermediate- and low-mass stars (e.g. Zinnecker et al. 1993; Gennaro et al. 2011; Pang et al. 2013). The underlying physical process is assumed to be dynam-

ical mass segregation (e.g. Bonnell & Davies 1998; Allison et al. 2009). Such effects are relevant within individual clusters, which are usually smaller than one element in our grid. However, since segregation timescales are of the order of several crossing times (e.g. de Grijs et al. 2002), dynamical mass segregation is too

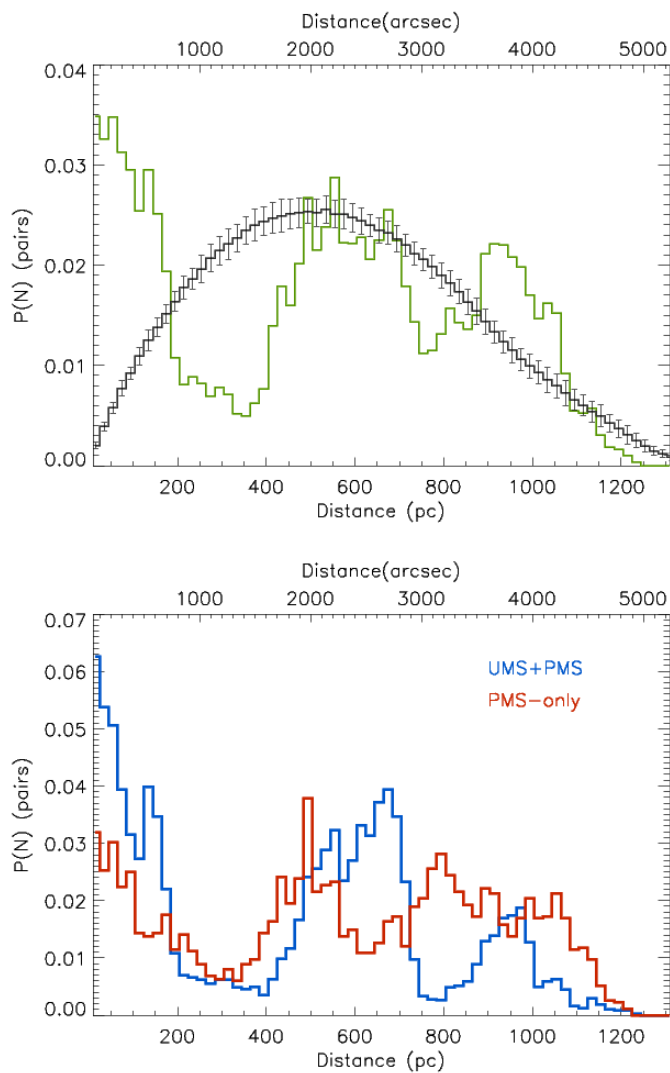


**Fig. 10. Top:** Normalised distance distribution for all possible grid pairs for the 208 PMS-only and UMS+PMS classified elements (green line), and for a same-size sample of randomly distributed unclassified elements (black line). **Bottom:** Same as the top panel, but separating the two classifications.

slow to explain the observed spatial distribution on the scales of the complexes N 44 and N 51.

In agreement with our results, the HTTP survey found that for the 30 Doradus region, the UMS stars also mostly concentrate in a few main population centres (Sabbi et al. 2016), while the PMS stellar distribution displays a larger spatial dispersion (Cignoni et al. 2015). Based on the distribution of PMS stars and the location of ionised filaments in 30 Doradus, Sabbi et al. (2016) find evidence of constructive feedback from massive stars igniting the birth of new generations of stars. In N 44, Chen et al. (2009) also reported evidence of triggered star formation. Triggering by massive stars could operate on larger spatial scales than mass segregation; it is thus a viable scenario for the different spatial distribution between PMS-only and UMS+PMS elements, since it could lead to the formation of less massive clusters or associations in the outskirts. This is observed in the Carina Nebula, where the currently ongoing star formation seems to produce only stars up to  $\sim 10 M_{\odot}$  (Gaczkowski et al. 2013).

Alternatively, the evaporation of bound clusters due to gas expulsion could also result in the observed spatial distribution of

classified elements. After a quick gas removal phase ( $\lesssim 1$  Myr), clusters are predicted to expand to half-mass radii  $\gtrsim 10$  pc (for masses  $\sim 5000 M_{\odot}$ ) within 10 Myr (Pfalzner et al. 2014). Crucially, they develop an extended stellar halo of ejected stars that can extend beyond 100 pc (Moeckel & Bate 2010). In the comparatively low stellar density environment of such halos, there will naturally be fewer UMS stars, thus increasing the likelihood of PMS-only classified elements in the cluster outskirts.

### 6.1.2. Individual regions

Several regions, associated with a large number of classified elements, are identified in Fig. 9. As described before, in N 51 and N 44, the UMS+PMS-classified elements are strongly clustered, whilst the PMS-only elements are often located in the outskirts of these regions. In both complexes significant dust and  $H\alpha$  emission is also observed. In N 44,  $H\alpha$  emission and the UMS+PMS-classified elements are spatially coincident, as would be expected since the ionising radiation from the UMS stars is the origin of the  $H\alpha$  emission. Two large substructures can be seen: the larger substructure near the centre corresponds to the associations LH 47 and LH 48, and the smaller substructure towards the south includes LH 49. To the east of N 51, a similarly strong overlap between  $H\alpha$  emission and classified elements is seen. To the west, the intense  $H\alpha$  emission traces a bubble-like shape, but the overlap with classified elements is patchy. Two OB associations, LH 51 and LH 54, are associated with this bubble (e.g. Book et al. 2009).

In addition to these complexes, the two most prominent concentrations of classified elements are located in the western part of N 148 and in Region A. N 148 is an intense and vigorous star-forming region (e.g. Ambrocio-Cruz et al. 2016) and is only partially covered by our analysis. Most grid elements are classified as PMS-only without a significant UMS population; this suggests the existence of a distributed population of intermediate- and low-mass PMS stars associated with N 148, identified here for the first time. Based on comparisons of the significance maps with synthetic clusters, some of the PMS-only grid elements seem very young ( $\sim 1$  Myr). The presence of significant dust and CO emission combined with the lack of extended  $H\alpha$  emission provides further evidence of a young population devoid of UMS stars.

The classified elements in Region A combine relatively weak PMS signatures with strong UMS signatures, suggesting an older age. The most prominent cluster in this area, NGC 2004, indeed has an age of  $\sim 20$  Myr (Niederhofer et al. 2015), resulting in a PMS population that is too faint to be reliably detected with the VMC data. Region A also lies in an area with no significant dust or  $H\alpha$  emission. This all hints at a comparatively old age of the dominant populations in the region, probably a result of the energetic feedback from massive stars that have significantly eroded the interstellar medium.

Another grouping of classified elements is found to the north-east of the emission nebula N 138. More specifically, the PMS-only and UMS+PMS-classified regions are spatially coincident with the  $H II$  regions N 138A and N 138C. In N 138A Indebetouw et al. (2004) found an ultracompact  $H II$  source, indicative of very young massive stars.

Our method for classifying young populations not only identifies all major star-forming complexes in tile LMC 7\_5, but also exposes their full extents and distribution for the first time.

**Table 3.** Number of PMS candidates in the whole LMC 7\_5 tile and individual prominent regions. The errors are calculated assuming grid elements are statistically independent.

	$N_{\text{PMS}}$
LMC 7_5	$2256 \pm 54$
N 44	$1000 \pm 38$
N 51	$379 \pm 22$
N 148	$238 \pm 20$
A	$112 \pm 13$
N 138	$74 \pm 9$

## 6.2. Quantitative analysis of the PMS populations

Using the residual maps, we calculate the number density of PMS candidates as well as the overall number of PMS candidates in the classified elements. Taking the mean density excess of the flagged boxes relevant for PMS populations (see Fig. 6) and multiplying it by the area covered by these boxes in the CMD, we derive the PMS number density. We obtain a mean PMS number density  $n_{\text{PMS}} = 12.7 \text{ stars arcmin}^{-2}$  over all elements classified as PMS-only or UMS+PMS. The uncertainty, estimated by analysing the density fluctuations in the residuals of non-classified elements, is  $\Delta n_{\text{PMS}} = 2.4 \text{ stars arcmin}^{-2}$ . Multiplying the PMS density by the solid angle of the grid element ( $\sim 1.4 \text{ arcmin}^2$ ), we derive the number of PMS candidates ( $N_{\text{PMS}}$ ). On average, there are  $N_{\text{PMS}} = 17.7 \pm 3.4$  per classified element.

In Fig. 9 we plot the PMS density contours. The highest density ( $40 \text{ stars arcmin}^{-2} \cong 0.18 \text{ stars pc}^{-2}$ ) is found within N 44. Large complexes contain multiple high-density peaks, displaying a hierarchical structure similar to that found for UMS stars by Sun et al. (2017a,b). Integrating over all classified elements and accounting for the overlap between neighbouring grid elements, we determine a total number of PMS candidates of  $2256 \pm 54$ . This result is a lower limit because the incompleteness in the VMC data at magnitudes typical of PMS stars is significant. Table 3 lists the number of PMS candidates for the whole pilot field as well as for the five regions described in the previous sections. Overall,  $\sim 80\%$  of all PMS candidates identified are located in one of these regions, with N 44 being the most populous.

For comparison, Meingast et al. (2016) estimated the entire young stellar population of the Orion A molecular cloud to have between 2300 and 3000 stars. Using a Kroupa IMF, this gives 300 to 390 stars with masses  $1 M_{\odot} \leq M_* \leq 4 M_{\odot}$ , which is the PMS mass range our method is sensitive to (see Fig. 6). The area covered by the Orion survey ( $18.3 \text{ deg}^2$ ) corresponds to  $4.5 \text{ arcmin}^2$  or 3.2 grid elements at the LMC distance. In the Carina Nebula complex, 8781 young stars were identified based on their NIR colour excess (Zeidler et al. 2016). Applying a Kroupa IMF to the same mass range gives  $\sim 1150$  stars that could potentially be identified as PMS with our method. This is comparable with our PMS count for the N 44 complex. We note, however, that this estimate includes only sources with an NIR colour excess. At the LMC distance, the area observed in Zeidler et al. (2016) corresponds to  $51.5 \text{ arcmin}^2$  or around 37 grid elements, which is approximately the area covered by the large group of classified elements in the centre of N 44. Incompleteness and crowding would obviously reduce the number of PMS sources we would be able to detect.

To obtain a more detailed view of the morphology of the PMS populations, we define PMS structures as regions enclosed by the lowest density contour in Fig. 9. We detect 31 structures in total, the most populous of which is located in N 44 and con-

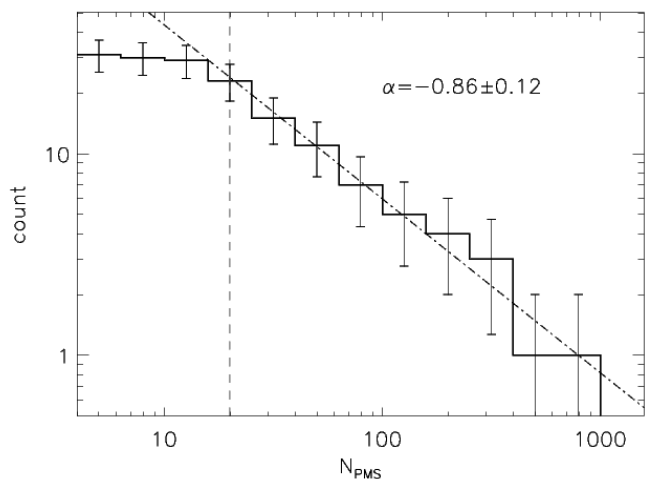


**Fig. 11.** Cumulative number distribution for the 31 PMS structures (0.2 dex bins). The vertical dashed line indicates the sensitivity limit, while the dash-dotted line represents a power law with a slope of  $-0.86$ . The error bars represent the Poissonian uncertainties.

tains  $\sim 670$  PMS candidates. Figure 11 shows the cumulative  $N_{\text{PMS}}$  distribution for the PMS structures. For  $N_{\text{PMS}} > 20$  the distribution can be approximated by a power law with a slope  $\alpha(N_{\text{PMS}}) = -0.86 \pm 0.12$ . Studies of cluster mass distributions have shown that high-mass clusters are less numerous than low-mass ones (e.g. Zhang & Fall 1999; Hunter et al. 2003; de Grijs & Goodwin 2008), with a slope  $\alpha(M) \sim -1$ . In a histogram using equal  $\log M$  intervals,  $\alpha(M) = -1$  is equivalent to a mass distribution function  $n(M)dm \propto M^{-\beta}dm$  with  $\beta = -2$ , which is the slope expected for a scale-free hierarchical star formation scenario governed by turbulence (e.g. Fleck 1996; Elmegreen 2008). Converting  $N_{\text{PMS}}$  obtained from our method into structure masses would yield very uncertain estimates because of the significant age dependence of the sensitivity limit of our VMC-based method (see Sec. 5.1). For predominantly “old” PMS populations,  $\alpha(M) > \alpha(N_{\text{PMS}})$  is expected, since a large fraction of PMS structures will have low PMS counts; for predominantly young PMS populations, we could expect  $\alpha(M) < \alpha(N_{\text{PMS}})$ . A more thorough discussion of the mass distribution should take the ages of the populations into account.

## 6.3. Comparison with dust emission maps

Since dust emission should be proportional to the product of dust mass and input stellar radiation (because of the energy balance between absorption and emission), one would expect a strong correlation between the number of young stars and dust emission. Bright FIR emission is usually associated with high star formation rates (see Casey et al. 2014 for a comprehensive overview); it originates from the radiation of the young stars that is processed by dust from the remnants of their natal molecular clouds and re-emitted at longer wavelengths. Skibba et al. (2012) have reported that some regions with bright dust emission in the MCs coincide with known star-forming regions. Moreover, in M33 only young structures ( $< 100 \text{ Myr}$ ) were found to correlate with FIR surface brightness (Javadi et al. 2017). Given that the presence of PMS stars is an indicator of recent star formation, we examined the relation with FIR emission in regions covered by the UMS+PMS and PMS-only classified elements.

We made use of data from the SAGE and HERITAGE surveys in six FIR bands ranging from  $70$  to  $500 \mu\text{m}$  (Meixner et al.

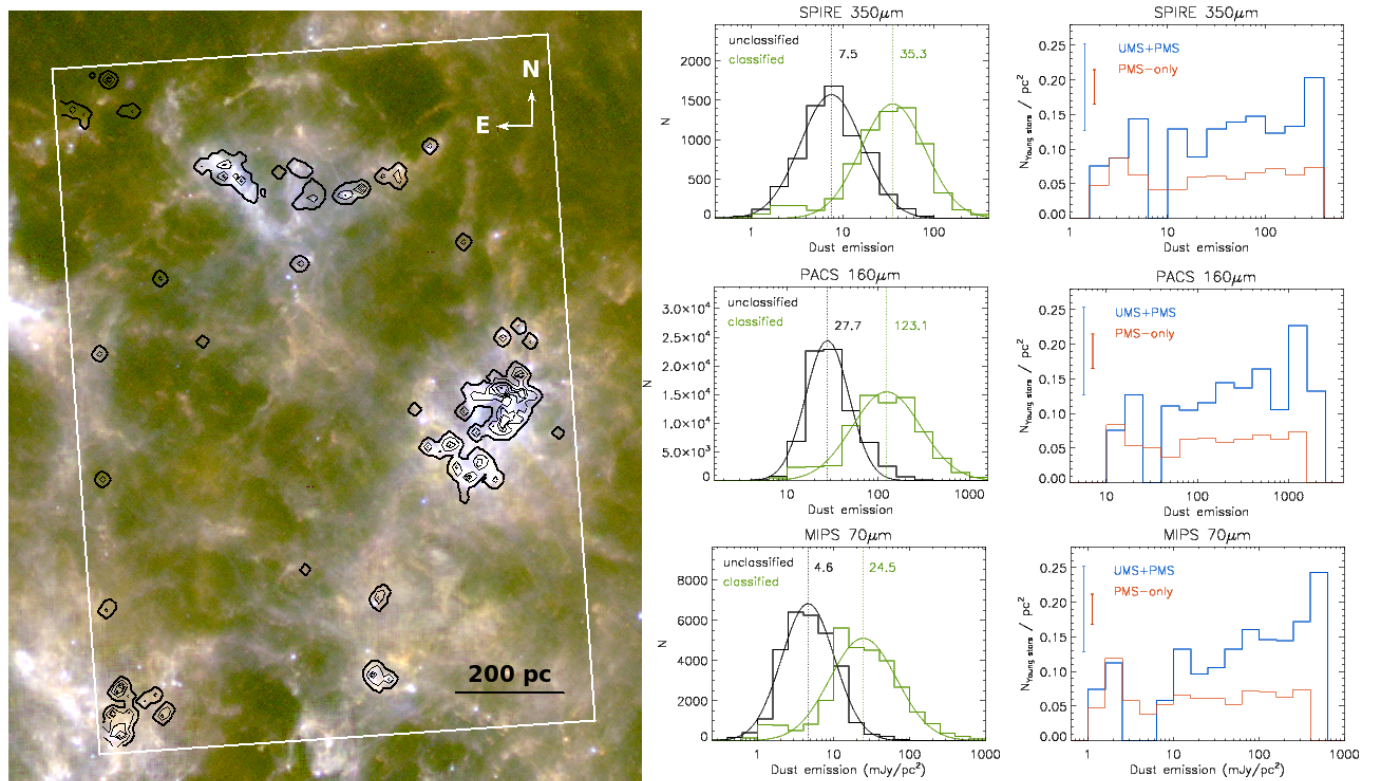


**Fig. 12.** **Left panel:** Three-colour composite image with *Spitzer* MIPS  $70\mu\text{m}$  in blue, *Herschel* PACS  $160\mu\text{m}$  in green, and *Herschel* SPIRE  $350\mu\text{m}$  in red; the density contours are the same as those in Fig. 9. **Middle panels:** Dust emission distribution for image pixels in areas covered by the UMS+PMS and PMS-only classified elements, and by the same number of randomly selected unclassified elements. A Gaussian fit is plotted and the mean of the fit is indicated. **Right panels:** Mean dust emission vs. young stars number density for the PMS and UMS+PMS classified elements. The error bars show the typical standard deviations within the dust emission bins.

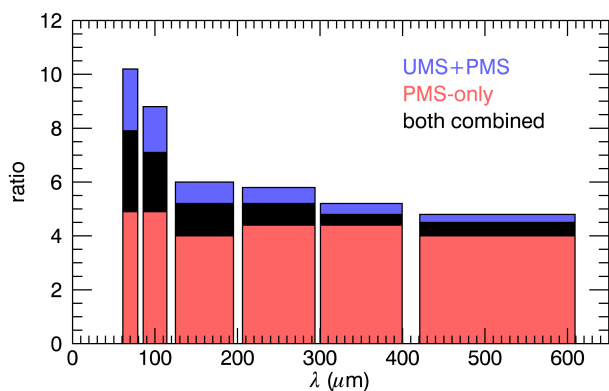


**Fig. 13.** Ratios of the mean dust emission observed for classified elements and the field average. The widths of the bars mimic the filter bandwidths.

2006, 2013). Figure 12 (left) shows the PMS density contours overplotted onto an RGB image ( $70$ ,  $160$  and  $350\mu\text{m}$ ) of the pilot field. PMS-only and UMS+PMS-classified elements are located along ridges and filamentary structures with bright dust emission. The only significant exceptions are Region A and some isolated PMS-only elements. As mentioned previously, the weak dust emission for Region A is in agreement with the inferred comparatively old age of the stellar populations.

The concentration of elements with PMS populations in regions with bright dust emission is explicitly shown in the middle

histograms of Fig. 12. The dust emission distributions for grid elements associated with PMS populations and a randomly selected sample of unclassified elements are clearly distinct; in particular, the strongest observed emission is always associated with young stellar populations.

Figure 12 (right) shows the dust emission versus the average number density of young stars for the same three FIR bands, separating PMS-only and UMS+PMS-classified grid elements. We computed UMS densities for the UMS+PMS elements similarly to the PMS densities (Sec. 6.2) to obtain the total density of young stars. We calculated the mean FIR emission for every classified element and grouped them in  $0.2$  dex bins; for every bin, the average number density of young stars was determined. For the UMS+PMS elements, we observe a relatively weak but consistent trend towards higher stellar number densities with increasing dust emission for all wavelengths. Hony et al. (2015) found a positive correlation between the number density of young stars (UMS and PMS stars identified using HST photometry (Gouliermis et al. 2006b)) and dust surface density in the prominent star-forming complex NGC 346 in the SMC. Their analysis, on scales comparable to the size of our grid elements, is in agreement with the trend in Figure 12 (right). For PMS-only elements, however, we do not observe an increase in stellar density with dust emission; less clustered low- and intermediate-mass PMS populations are likely more affected by the limitations of the VMC data.

Depending on the wavelength, the emission associated with the UMS+PMS and PMS-only classified elements is between four and eight times brighter than the field average (Fig. 13); the strongest enhancement is found for the shorter wavelengths.

Furthermore, the ratios for the PMS-only sample (red) are essentially independent of the wavelength, while the ratio for the UMS+PMS sample (blue) increases significantly towards shorter wavelengths. This is evidence that the dust is heated primarily by the young massive UMS stars, while the PMS populations contribute very little. This is consistent with studies that found that warm dust follows the distribution of massive stars in the LMC (Bernard et al. 2008), as well as in Galactic star-forming complexes (Preibisch et al. 2012; Roccatagliata et al. 2013). As a comparison, for the UMS-only classified elements (not shown), the dust emission is between 1.3 and 1.8 times higher than the pilot field average. The analysis in this section confirms the important role that young UMS stars play in heating the dust.

## 7. Summary and conclusions

We presented a method for identifying PMS populations ( $\geq 1 M_{\odot}$ ) using data from the VMC survey. The method applies a Hess diagram analysis in the  $K_s/(Y - K_s)$  space, including corrections for reddening and completeness, to distinguish young stellar populations from the underlying field; this analysis is performed independently on individual fixed-size spatial grid elements. Young populations are identified as density excesses (with respect to the field population) in pre-defined regions of the differential Hess diagrams. Depending on the location of these density excesses with respect to theoretical expectations (i.e. isochrones), we classify the population within a grid element into one of the four classes: PMS-only (population of young low-mass stars), UMS+PMS (young population with well-sampled IMF across the mass range), UMS-only (predominantly older population dominated by a prominent main-sequence population), and “old” (population that displays a significant contribution from evolved stars, in particular populating the red giant branch).

We applied our method to a  $\sim 1.5 \text{ deg}^2$  VMC pilot field (LMC 7\_5) and summarise our findings below.

- Tests with synthetic clusters explore the sensitivity of the method in the age range 1 Myr – 1 Gyr and the mass range  $250 M_{\odot} - 3000 M_{\odot}$ . We find that PMS populations can be identified up to an age of  $\sim 10$  Myr for cluster masses  $> 1000 M_{\odot}$ . Beyond 10 Myr, any remaining PMS populations are below the VMC sensitivity limit. The sensitivity increases towards younger ages: PMS populations with ages  $\leq 2$  Myr can be detected for clusters with masses down to  $250 M_{\odot}$ .
- We detected a total number of  $2256 \pm 54$  PMS stars in the pilot field. The most populous region is the N44 complex, which has  $1000 \pm 38$  PMS stars. This estimate must be taken as a lower limit because the VMC data are incomplete and our method has a sensitivity limit.
- The spatial distribution of elements with PMS populations is clearly inhomogeneous and clustered. UMS+PMS elements are almost exclusively found in large groups, while the PMS-only elements are more dispersed and often located in the outskirts of large star-forming complexes.
- Large star-forming complexes consist of multiple high stellar density peaks, with the highest densities found in the N44 complex. Overall, we detect 31 PMS structures whose number distribution can be approximated by a power law with a slope of  $-0.86 \pm 0.12$ . A mass distribution with this slope would be broadly consistent with a hierarchical star formation scenario governed by turbulence.
- The PMS populations are mostly located along ridges with intense dust emission in the FIR ( $70 - 500 \mu\text{m}$ ). We observe a correlation between the dust emission and the number of young stars for the UMS+PMS elements. This is not the case for the PMS-only elements that lack UMS stars. Dust emission is around four to eight times brighter for the UMS+PMS elements than in quiescent regions; at the shortest wavelengths, the emission can be as much as ten times brighter. This is likely due to dust heating by the radiation from the young UMS stars.
- Our analysis recovers all known star formation complexes in this field, and for the first time reveals their true spatial extent.
- In the south-eastern corner of LMC 7\_5, we discovered a significant intermediate- and low-mass PMS population that is likely associated with the wider N 148 star-forming complex. Comparison with synthetic cluster Hess CMDs suggests a very young age ( $\sim 1$  Myr) for this population. This population is co-spatial with significant CO emission.

Our method clearly shows the potential of the VMC survey to identify and characterise intermediate- and low-mass young stellar populations on the scale of the whole Magellanic system. We are working on applying our method to other LMC and SMC VMC tiles.

*Acknowledgements.* This work is based on observations obtained with VISTA under ESO-program ID 179.B-2003. We thank the Cambridge Astronomy Survey Unit (CASU) and the Wide Field Astronomy Unit (WFAU) in Edinburgh for providing calibrated data products through the support of the Science and Technology Facility Council (STFC). This research has made use of the SIMBAD database, operated at CDS, Strasbourg, France, and of the NASA Astrophysics Data System (ADS) bibliographic services. We thank Marta Sewilo for sharing her extensive compilation of LMC images and catalogues. Viktor Zivkov acknowledges studentships from ESO and the Faculty of Natural Sciences, Keele University, UK. We thank the anonymous referee for the constructive comments.

## References

- Allison, R. J., Goodwin, S. P., Parker, R. J., et al. 2009, *ApJ*, 700, L99  
 Ambrocio-Cruz, P., Le Coarer, E., Rosado, M., et al. 2016, *MNRAS*, 457, 2048  
 Baraffe, I., Homeier, D., Allard, F., & Chabrier, G. 2015, *A&A*, 577, A42  
 Beccari, G., Petr-Gotzens, M. G., Boffin, H. M. J., et al. 2017, *A&A*, 604, A22  
 Bernard, J.-P., Reach, W. T., Paradis, D., et al. 2008, *AJ*, 136, 919  
 Besla, G., Kallivayalil, N., Hernquist, L., et al. 2012, *MNRAS*, 421, 2109  
 Bica, E., Bonatto, C., Dutra, C. M., & Santos, J. F. C. 2008, *MNRAS*, 389, 678  
 Bok, B. J. 1964, in *IAU Symposium, Vol. 20, The Galaxy and the Magellanic Clouds*, ed. F. J. Kerr, 335  
 Bonnell, I. A. & Davies, M. B. 1998, *MNRAS*, 295, 691  
 Book, L. G., Chu, Y.-H., Gruendl, R. A., & Fukui, Y. 2009, *AJ*, 137, 3599  
 Bressan, A., Marigo, P., Girardi, L., et al. 2012, *MNRAS*, 427, 127  
 Carlson, L. R., Sewilo, M., Meixner, M., Romita, K. A., & Lawton, B. 2012, *A&A*, 542, A66  
 Casey, C. M., Narayanan, D., & Cooray, A. 2014, *Phys. Rep.*, 541, 45  
 Catelan, M., Minniti, D., Lucas, P. W., et al. 2011, in *RR Lyrae Stars, Metal-Poor Stars, and the Galaxy*, ed. A. McWilliam, Vol. 5, 145  
 Chen, C.-H. R., Chu, Y.-H., Gruendl, R. A., Gordon, K. D., & Heitsch, F. 2009, *ApJ*, 695, 511  
 Cignoni, M., Sabbi, E., van der Marel, R. P., et al. 2015, *ApJ*, 811, 76  
 Cioni, M.-R. L., Clementini, G., Girardi, L., et al. 2011, *A&A*, 527, A116  
 Contreras Peña, C., Lucas, P. W., Froebrich, D., et al. 2014, *MNRAS*, 439, 1829  
 Cook, D. O., Dale, D. A., Johnson, B. D., et al. 2014, *MNRAS*, 445, 881  
 Cross, N. J. G., Collins, R. S., Mann, R. G., et al. 2012, *A&A*, 548, A119  
 Da Rio, N., Gouliermis, D. A., & Henning, T. 2009, *ApJ*, 696, 528  
 de Grijs, R. & Anders, P. 2006, *MNRAS*, 366, 295  
 de Grijs, R. & Bono, G. 2015, *AJ*, 149, 179  
 de Grijs, R., Gilmore, G. F., Johnson, R. A., & Mackey, A. D. 2002, *MNRAS*, 331, 245  
 de Grijs, R. & Goodwin, S. P. 2008, *MNRAS*, 383, 1000  
 de Grijs, R., Wicker, J. E., & Bono, G. 2014, *AJ*, 147, 122  
 De Marchi, G., Beccari, G., & Panagia, N. 2013, *ApJ*, 775, 68

- Elmegreen, B. G. 2008, in *Astronomical Society of the Pacific Conference Series*, Vol. 388, *Mass Loss from Stars and the Evolution of Stellar Clusters*, ed. A. de Koter, L. J. Smith, & L. B. F. M. Waters, 249
- Fleck, Jr., R. C. 1996, *ApJ*, 458, 739
- Gaczkowski, B., Preibisch, T., Ratzka, T., et al. 2013, *A&A*, 549, A67
- Gennaro, M., Brandner, W., Stolte, A., & Henning, T. 2011, *MNRAS*, 412, 2469
- Gilmozzi, R., Kinney, E. K., Ewald, S. P., Panagia, N., & Romaniello, M. 1994, *ApJ*, 435, L43
- Girardi, L., Goudfrooij, P., Kalirai, J. S., et al. 2013, *MNRAS*, 431, 3501
- Girardi, L. & Salaris, M. 2001, *MNRAS*, 323, 109
- Glatt, K., Grebel, E. K., & Koch, A. 2010, *A&A*, 517, A50
- González-Fernández, C., Hodgkin, S. T., Irwin, M. J., et al. 2018, *MNRAS*, 474, 5459
- Gordon, K. D., Meixner, M., Meade, M. R., et al. 2011, *AJ*, 142, 102
- Gouliermis, D., Brandner, W., & Henning, T. 2006a, *ApJ*, 636, L133
- Gouliermis, D., Kontizas, M., Kontizas, E., & Korakitis, R. 2003, *A&A*, 405, 111
- Gouliermis, D. A. 2012, *Space Sci. Rev.*, 169, 1
- Gouliermis, D. A. 2018, *PASP*, 130, 072001
- Gouliermis, D. A., Dolphin, A. E., Brandner, W., & Henning, T. 2006b, *ApJS*, 166, 549
- Gouliermis, D. A., Dolphin, A. E., Robberto, M., et al. 2011, *ApJ*, 738, 137
- Gouliermis, D. A., Henning, T., Brandner, W., et al. 2007, *ApJ*, 665, L27
- Gruendl, R. A. & Chu, Y.-H. 2009, *ApJS*, 184, 172
- Henize, K. G. 1956, *ApJS*, 2, 315
- Hony, S., Gouliermis, D. A., Galliano, F., et al. 2015, *MNRAS*, 448, 1847
- Hunter, D. A., Elmegreen, B. G., Dupuy, T. J., & Mortonson, M. 2003, *AJ*, 126, 1836
- Indebetouw, R., Johnson, K. E., & Conti, P. 2004, *AJ*, 128, 2206
- Irwin, M. J., Lewis, J., Hodgkin, S., et al. 2004, in *Proc. SPIE*, Vol. 5493, *Optimizing Scientific Return for Astronomy through Information Technologies*, ed. P. J. Quinn & A. Bridger, 411–422
- Javadi, A., van Loon, J. T., Khosroshahi, H. G., et al. 2017, *MNRAS*, 464, 2103
- Kerber, L. O., Girardi, L., Rubele, S., & Cioni, M.-R. 2009, *A&A*, 499, 697
- Kroupa, P. 2001, *MNRAS*, 322, 231
- Kroupa, P. 2002, *Science*, 295, 82
- Liu, Q., de Grijs, R., Deng, L. C., et al. 2009a, *MNRAS*, 396, 1665
- Liu, Q., de Grijs, R., Deng, L. C., Hu, Y., & Beaulieu, S. F. 2009b, *A&A*, 503, 469
- Lucke, P. B. & Hodge, P. W. 1970, *AJ*, 75, 171
- Massey, P., Parker, J. W., & Garmany, C. D. 1989a, *AJ*, 98, 1305
- Massey, P., Silkey, M., Garmany, C. D., & Degioia-Eastwood, K. 1989b, *AJ*, 97, 107
- Meingast, S., Alves, J., Mardones, D., et al. 2016, *A&A*, 587, A153
- Meixner, M., Gordon, K. D., Indebetouw, R., et al. 2006, *AJ*, 132, 2268
- Meixner, M., Panuzzo, P., Roman-Duval, J., et al. 2013, *AJ*, 146, 62
- Moeckel, N. & Bate, M. R. 2010, *MNRAS*, 404, 721
- Mollá, M., García-Vargas, M. L., & Bressan, A. 2009, *MNRAS*, 398, 451
- Niederhofer, F., Bastian, N., Kozhurina-Platais, V., et al. 2017, *MNRAS*, 465, 4159
- Niederhofer, F., Hilker, M., Bastian, N., & Silva-Villa, E. 2015, *A&A*, 575, A62
- Paczynski, B. & Stanek, K. Z. 1998, *ApJ*, 494, L219
- Panagia, N., Romaniello, M., Scuderi, S., & Kirshner, R. P. 2000, *ApJ*, 539, 197
- Pang, X., Grebel, E. K., Allison, R. J., et al. 2013, *ApJ*, 764, 73
- Pei, Y. C., Fall, S. M., & Hauser, M. G. 1999, *ApJ*, 522, 604
- Pfalzner, S., Parmentier, G., Steinhausen, M., Vincke, K., & Menten, K. 2014, *ApJ*, 794, 147
- Piatti, A. E., Guandalini, R., Ivanov, V. D., et al. 2014, *A&A*, 570, A74
- Piatti, A. E., Ivanov, V. D., Rubele, S., et al. 2016, *MNRAS*, 460, 383
- Pilbratt, G. L., Riedinger, J. R., Passvogel, T., et al. 2010, *A&A*, 518, L1
- Popescu, B., Hanson, M. M., & Elmegreen, B. G. 2012, *ApJ*, 751, 122
- Preibisch, T., Roccatagliata, V., Gaczkowski, B., & Ratzka, T. 2012, *A&A*, 541, A132
- Rice, T. S., Reipurth, B., Wolk, S. J., Vaz, L. P., & Cross, N. J. G. 2015, *AJ*, 150, 132
- Roccatagliata, V., Preibisch, T., Ratzka, T., & Gaczkowski, B. 2013, *A&A*, 554, A6
- Rubele, S., Girardi, L., Kerber, L., et al. 2015, *MNRAS*, 449, 639
- Rubele, S., Girardi, L., Kozhurina-Platais, V., Goudfrooij, P., & Kerber, L. 2011, *MNRAS*, 414, 2204
- Rubele, S., Kerber, L., Girardi, L., et al. 2012, *A&A*, 537, A106
- Russell, S. C. & Dopita, M. A. 1992, *ApJ*, 384, 508
- Sabbi, E., Anderson, J., Lennon, D. J., et al. 2013, *AJ*, 146, 53
- Sabbi, E., Lennon, D. J., Anderson, J., et al. 2016, *ApJS*, 222, 11
- Schneider, F. R. N., Ramírez-Agudelo, O. H., Trammer, F., et al. 2018a, *ArXiv e-prints* [arXiv:1807.03821]
- Schneider, F. R. N., Sana, H., Evans, C. J., et al. 2018b, *Science*, 359, 69
- Skibba, R. A., Engelbracht, C. W., Aniano, G., et al. 2012, *ApJ*, 761, 42
- Skrutskie, M. F., Cutri, R. M., Stiening, R., et al. 2006, *AJ*, 131, 1163
- Smith, R. C., Points, S. D., Chu, Y.-H., et al. 2005, in *Bulletin of the American Astronomical Society*, Vol. 37, *American Astronomical Society Meeting Abstracts*, 1200
- Spezzi, L., De Marchi, G., Panagia, N., Sicilia-Aguilar, A., & Ercolano, B. 2012, *MNRAS*, 421, 78
- Stanimirović, S., Staveley-Smith, L., & Jones, P. A. 2004, *ApJ*, 604, 176
- Subramanian, S. & Subramaniam, A. 2009, *A&A*, 496, 399
- Sun, N.-C., de Grijs, R., Cioni, M.-R. L., et al. 2018, *ApJ*, 858, 31
- Sun, N.-C., de Grijs, R., Subramanian, S., et al. 2017a, *ApJ*, 849, 149
- Sun, N.-C., de Grijs, R., Subramanian, S., et al. 2017b, *ApJ*, 835, 171
- Sutherland, W., Emerson, J., Dalton, G., et al. 2015, *A&A*, 575, A25
- Tatton, B. L., van Loon, J. T., Cioni, M.-R., et al. 2013, *A&A*, 554, A33
- Tout, C. A., Livio, M., & Bonnell, I. A. 1999, *MNRAS*, 310, 360
- van der Marel, R. P. & Cioni, M.-R. L. 2001, *AJ*, 122, 1807
- Werner, M. W., Roellig, T. L., Low, F. J., et al. 2004, *ApJS*, 154, 1
- Westerlund, B. 1961, *Uppsala Astronomical Observatory Annals*, 5, 1
- Wong, T., Hughes, A., Ott, J., et al. 2011, *ApJS*, 197, 16
- Zaritsky, D., Harris, J., Thompson, I. B., & Grebel, E. K. 2004, *AJ*, 128, 1606
- Zaritsky, D., Harris, J., Thompson, I. B., Grebel, E. K., & Massey, P. 2002, *AJ*, 123, 855
- Zeidler, P., Preibisch, T., Ratzka, T., Roccatagliata, V., & Petr-Gotzens, M. G. 2016, *A&A*, 585, A49
- Zhang, Q. & Fall, S. M. 1999, *ApJ*, 527, L81
- Zinnecker, H., McCaughrean, M. J., Rayner, J. T., Wilking, B. A., & Moneti, A. 1993, in *Reviews in Modern Astronomy*, Vol. 6, *Reviews in Modern Astronomy*, ed. G. Klare, 191–208

## Appendix A: Spatial distribution of the older population

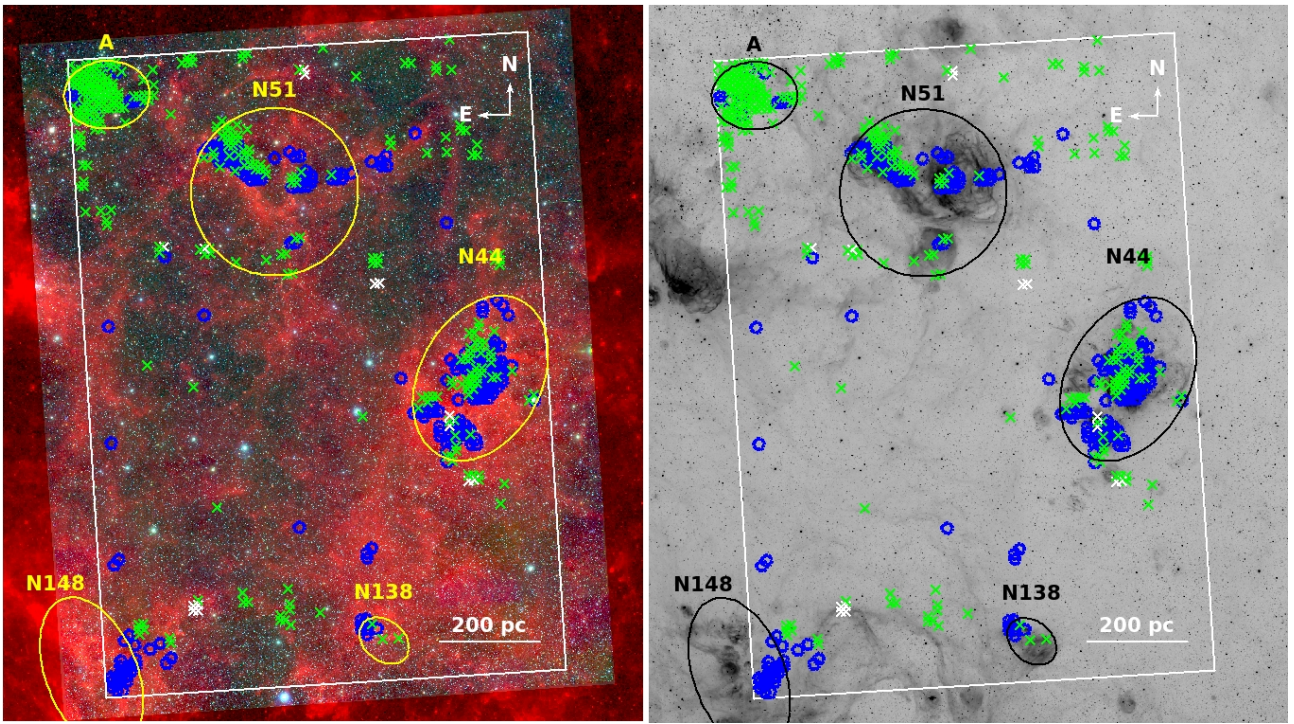
In Sec. 6.1 we analysed the spatial distribution of elements showing a PMS signature. We found especially pronounced clustering for UMS+PMS-classified grid elements, which represent young and relatively massive populations. Here we investigate the spatial distribution of the 298 grid elements classified as UMS-only. They contain comparatively old populations (10 – 300 Myr; see Sec. 4).

Figure A.1 shows the location of the grid elements classified as UMS-only and “old”. Their spatial distribution is more scattered across the pilot field than the UMS+PMS elements. Consequently, more UMS-only elements are either isolated or located in small groups outside the known complexes. The concentration of UMS-only elements in region A is noticeable and is further confirmation of the comparatively older age of this population. The 14 grid elements classified as “old” are scattered across the field and are neither co-spatial with young grid elements, nor with any significant dust or  $H\alpha$  emission. Twelve of them seem associated with known LMC clusters (Bica et al. 2008).

Fig. A.2 is equivalent to Fig. 10 (bottom), but shows the distance distributions for all possible pairs of UMS+PMS and UMS-only classified elements. Some clustering is present for UMS-only elements, but it is much less pronounced than that for the UMS+PMS classified elements; UMS-only elements show a comparatively smooth distribution. This is in agreement with the temporal evolution of young stellar structures, which are observed to disperse on long timescales (e.g. Sun et al. 2017a).

## Appendix B: Reddening correction

Before comparing a grid element with its corresponding control field, we redden the control field according to the distribution of RC stars in the grid element (see Sec. 3.3). Figure B.1 shows how this correction is performed. The blue line represents the cumulative colour distribution of RC stars in the control field. Since the control field combines several grid elements, it contains many RC stars. This creates a very smooth distribution. The steep slope indicates a compact RC with little differential reddening. The black line shows the cumulative distribution for



**Fig. A.1.** **Left:** Three-colour composite image with VMC  $Y$  (blue) and  $K_s$  bands (green), and *Spitzer* IRAC  $8.0\mu\text{m}$  (see also Fig. 9). Green and white crosses mark the locations of elements classified as UMS and “old”, respectively. The UMS+PMS and PMS-only classified elements are included as blue circles to facilitate comparison. **Right:** Same as the left panel, but using an inverted grey-scale image of the  $H\alpha$  emission.

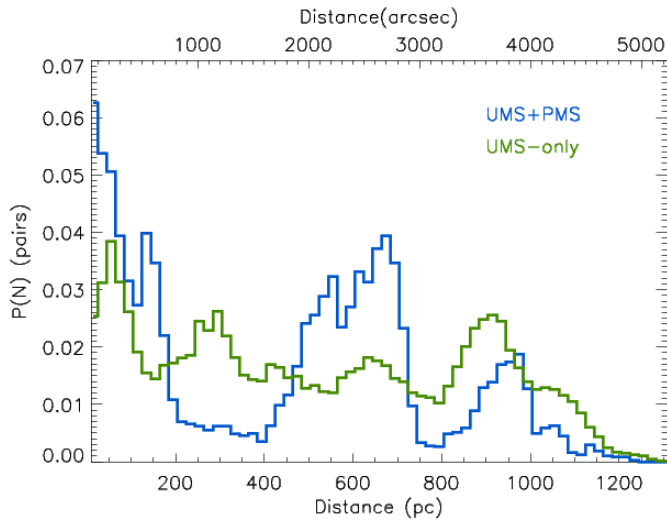


**Fig. A.2.** Normalised distance distribution for all possible grid element pairs classified as UMS+PMS (blue) and UMS-only (green) (see also Fig 10).

the grid element being studied. Its slope is shallower because the RC is more spread out. Especially the top  $\sim 25\%$  of the most strongly reddened stars suggests substantial differential reddening.

After the reddening correction is applied to the control field population, its RC distribution (red line) closely follows the grid element RC distribution. Differential reddening is accounted for, which would not have been possible by simply adopting a fixed reddening value for the control field stars.

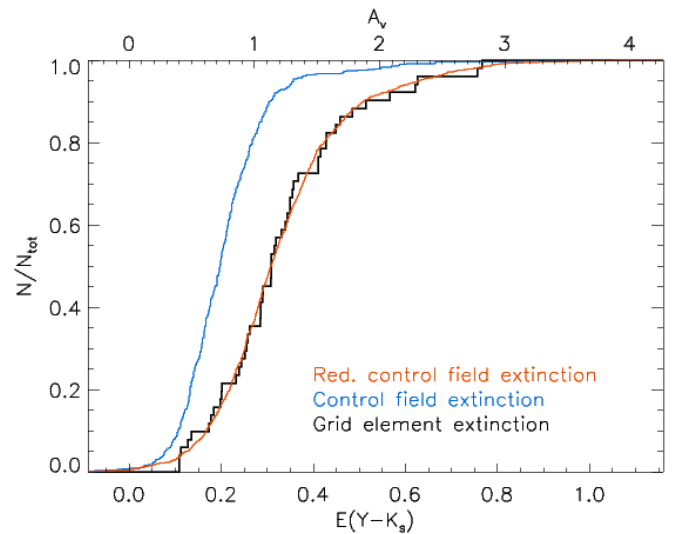


**Fig. B.1.** Cumulative colour distribution of RC stars for the grid element under investigation (black line), and for the corresponding control field before and after the reddening correction (blue and red lines, respectively). RC stars are defined by the RC selection box in Fig. 3. The intrinsic RC colour adopted is  $(Y-K_s)_0 = 0.84$  mag (Tatton et al. 2013).

## Appendix C: Images of selected star-forming complexes

Figure C.1 presents close-up views of the three most populous regions in this LMC tile (see Table 3). It shows ionised gas ( $H\alpha$ ), stellar content ( $K_s$  band), and hot dust ( $8\mu\text{m}$ ), together with the PMS density contours as calculated in Sec. 6.2.



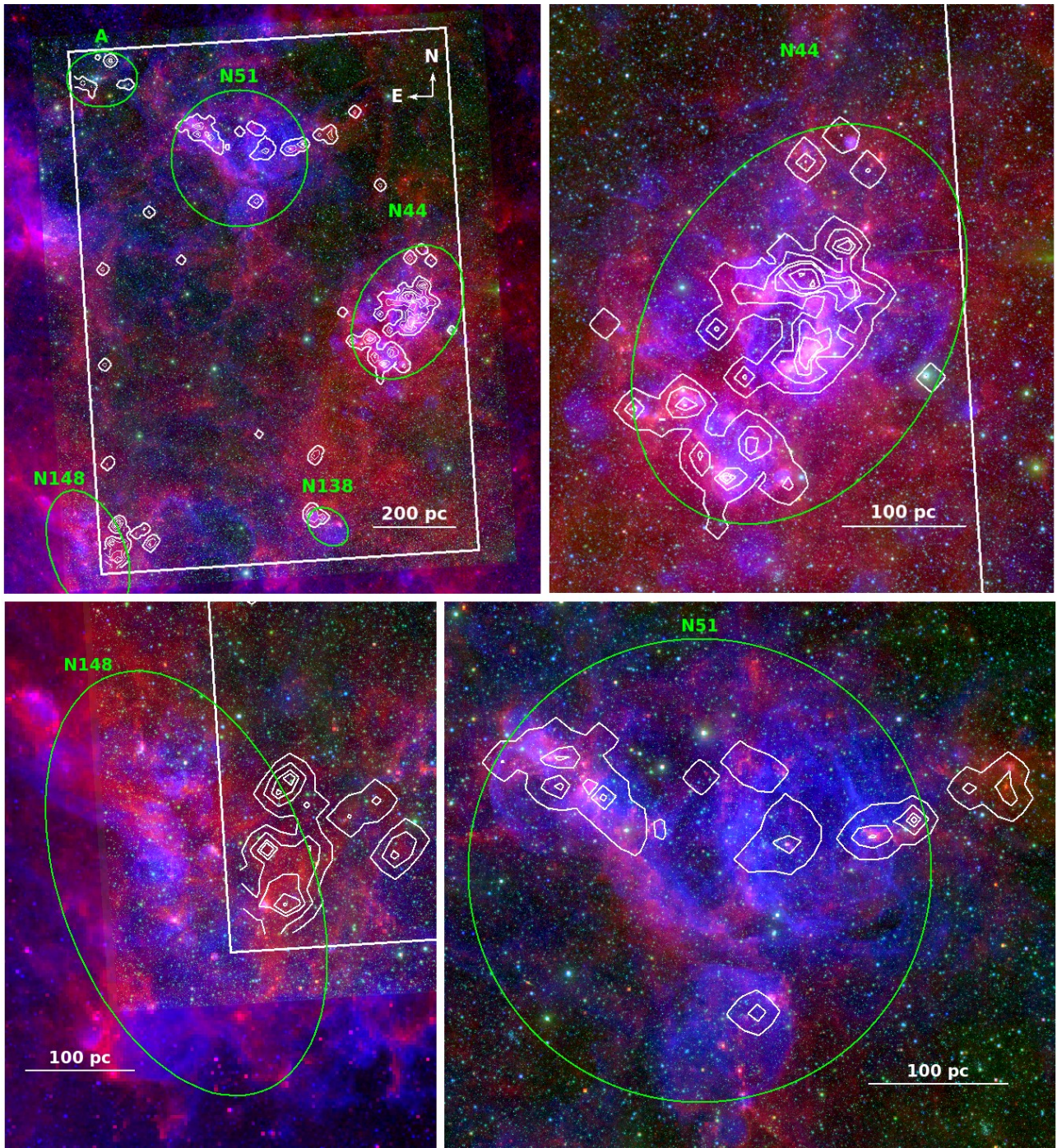


**Fig. C.1.** Three-colour composite image (top left) of the analysed area with  $H\alpha$  emission in blue,  $K_s$  ( $2.15\ \mu\text{m}$ ) in green, and *Spitzer* IRAC  $8\ \mu\text{m}$  in red. Regions and contours are the same as in Fig. 9. Other panels show enlarged views of selected star-forming complexes: N 44 (top right), N 148 (bottom left), and N 51 (bottom right).